THE JOURNAL OF BIOLOGICAL CHEMISTRY VOL. 289, NO. 39, pp. 26829–26846, September 26, 2014

A Residue-specific Shift in Stability and Amyloidogenicity of Antibody Variable Domains*

Received for publication, May 16, 2014, and in revised form, July 28, 2014 Published, JBC Papers in Press, August 5, 2014, DOI 10.1074/jbc.M114.582247

Cardine N. Nokwe[‡], Martin Zacharias[§], Hisashi Yagi[¶‖], Manuel Hora[‡], Bernd Reif[‡], Yuji Goto[‖], and Johannes Buchner[‡1]

From the [‡]Center for Integrated Protein Science, Department of Chemie, Technische Universität München, Lichtenbergstrasse 4, D-85747 Garching, Germany, the [§]Center for Integrated Protein Science, Department of Physik, Technische Universität München, James-Franck-Strasse 1, D-85748 Garching, Germany, the [¶]Department of Chemistry and Biotechnology, Graduate School of Engineering and Center for Research on Green Sustainable Chemistry, Tottori University, 4-101 Koyamatyo-minami, Tottori 680-8550, Japan, and the [‖]Division of Protein Structural Biology, Institute for Protein Research, Osaka University, 3-2 Yamadaoka, Suita, Osaka 565-0871, Japan

Background: Amyloid fibrils of variable (V_L) domains are the main cause of death in light chain amyloidosis.
Results: Conserved V_L residue 2 is crucial for structural integrity and amyloidogenicity of $V_L\kappa$ domains.
Conclusion: Our data reveal novel insights into the architecture of variable domains in general and the prerequisite for fibrillation.
Significance: This is important for understanding the principles of antibody structure and amyloidogenicity.

Variable (V) domains of antibodies are essential for antigen recognition by our adaptive immune system. However, some variants of the light chain V domains (V_L) form pathogenic amyloid fibrils in patients. It is so far unclear which residues play a key role in governing these processes. Here, we show that the conserved residue 2 of V_L domains is crucial for controlling its thermodynamic stability and fibril formation. Hydrophobic side chains at position 2 stabilize the domain, whereas charged residues destabilize and lead to amyloid fibril formation. NMR experiments identified several segments within the core of the V_L domain to be affected by changes in residue 2. Furthermore, molecular dynamic simulations showed that hydrophobic side chains at position 2 remain buried in a hydrophobic pocket, and charged side chains show a high flexibility. This results in a predicted difference in the dissociation free energy of ~10 kJ mol^{-1}, which is in excellent agreement with our experimental values. Interestingly, this switch point is found only in V_L domains of the κ family and not in $V_L\lambda$ or in V_H domains, despite a highly similar domain architecture. Our results reveal novel insight into the architecture of variable domains and the prerequisites for formation of amyloid fibrils. This might also contribute to the rational design of stable variable antibody domains.

Antibodies consist of structurally highly homologous domains all sharing the immunoglobulin fold. This tertiary structure is characterized by two β-sheets that are connected by a conserved disulfide bridge and form a β-barrel structure. In the variable domains, the anti-parallel β-pleated sheets include nine β-strands in a 4 + 5 orientation (ABE(D/C)C′C″FG) (1), whereas those of the constant domains are made up of seven β-strands in a 4 + 3 orientation (ABE(D/C)FG) (2). In the variable domains, this framework structure is expanded by three variable loops (CDR[2] 1–3) that mediate antigen recognition. The principles that govern the stability of the variable domains are of special importance, as loops of different lengths and composition have to be tolerated. To achieve this, the amino acid composition of the framework is highly conserved at most positions. Single substitutions in variable domains can have deleterious effects, seen in some patients with monoclonal gammopathy or clonal B cell dyscrasias. In these patients, antibody variants are pathologically deposited in a fatal illness called light chain deposition disease (3, 4) and systemic amyloid light chain (AL) amyloidosis (5, 6). Analysis of proteins isolated from AL patient biopsies showed that the main constituent of amyloid deposits is the variable domain of the light chain (V_L) (7, 8). The basis of the disease is the overproduction of unpaired antibody light chains (LCs), which are secreted into the bloodstream and taken up by multiple organs and tissues where they aggregate, severely compromising the functions of the affected organs and ultimately leading to death (9, 10). AL amyloidosis remains the most common and most fatal systemic amyloidosis in western countries (7, 11).

Despite the high similarity between the V_L and V_H domains, V_H is less susceptible to amyloid fibril formation (12). Furthermore, why some V_Ls form amyloids and others do not still remains largely enigmatic. In general, it is therefore not clear which residues are of special importance for the structural integrity of the V_L domain. As the C_L domain is not involved in the deposits, it seems that structural elements exist that protect it from misfolding (13), whereas some factors within the V_L

* This work was supported by a grant from the Deutsche Forschungsgemeinschaft (to J. B.) and by a grant from the Bundesministerium für Bildung und Forschung (BMBF) within the framework of the research network GERAMY (to B. R.).
[1] To whom correspondence should be addressed. Tel.: 49-89-289-13340; Fax: 49-89-289-13345; E-mail: johannes.buchner@tum.de.

[2] The abbreviations used are: CDR, complementarity-determining region; AL, antibody light chain; TEM, transmission electron microscopy; LC, light chain; MD, molecular dynamics; r.m.s.d., root mean square deviation; PDB, Protein Data Bank; GdmCl, guanidinium chloride; US, umbrella sampling; ANS, 1-anilino-8-naphthalene sulfonate; V, variable; ThT, thioflavin T.

domain might predispose it to the disease state. Highly conserved consensus sequences within the framework region are potentially important elements in this respect. A striking feature of variable domains is the conserved N terminus of β-strand A (FWR1). However, the role of the N-terminal residues of the LC on domain structure, stability, and amyloidogenic potential is still unresolved.

In this study, we performed a detailed analysis of the importance of the conserved N-terminal residues for the structural integrity, the conformational stability, and amyloidogenicity of variable domains. With biophysical approaches including CD, fluorescence, NMR, and molecular dynamics (MD) simulations, we demonstrate that specifically residue 2 affects the conformational integrity and is a key element controlling its amyloidogenic properties. This reveals novel insights into the architecture of antibody variable domains.

EXPERIMENTAL PROCEDURES

Oligonucleotides (primers) were purchased from MWG Biotec. Ultrapure GdmCl was obtained from Sigma. All other chemicals were purchased from Merck. The concentrations of GdmCl solutions were determined from refractive indices (14). Unless stated otherwise, all measurements were carried out at 25 °C (pH 7.4) in PBS buffer.

Cloning, Mutagenesis, Expression, and Purification of the Variable Domain Variants—The MAK33 $V_L\kappa$ wild type encoding plasmid was obtained as published previously (15). 1OPG $V_L\kappa$, 1AQK $V_L\lambda$, and 1VGE V_H wild type sequences cloned into a pET28b vector between the NcoI and HindIII restriction sites were purchased from Geneart AG (Regensburg, Germany). Single, double, and triple point mutants were generated with QuikChange mutagenesis PCR with forward and reverse primers carrying the target mutation. Inserts of the wild type, single point, and double point mutants in the pET28b vector were used as PCR templates for the generation of single, double, and triple point mutants, respectively. The PCR was followed by digestion of template DNA with DpnI enzyme (New England Biolabs) for 1 h at 37 °C. The PCR product was then transformed through a heat shock-dependent transformation into competent *Escherichia coli* Mach1 cells. Positive clones were selected on kanamycin LB plates overnight at 37 °C. Plasmid DNA from a single colony was isolated with the Wizard Plus SV Miniprep kit (Promega) and sequenced using the T7 forward or pET-RP sequencing primer by Eurofins MWG Operon to verify the desired mutation. All MAK33 $V_L\kappa$, 1OPG $V_L\kappa$, 1AQK $V_L\lambda$, and 1VGE V_H variants were expressed and purified as described previously (15, 16). In brief, the plasmid was transformed into *E. coli* BL21(DE3)-star cells (for $V_L\kappa$ and λ variants) or in *E. coli* JM109 cells (for V_H variants) for expression at 37 °C. At an A_{600} of 0.6–0.8, expression was induced using 1 mM isopropyl β-D-thiogalactopyranoside. Cells were harvested after overnight growth, and inclusion bodies were prepared as described previously (17, 18). The pellet was solubilized and unfolded in 25 mM Tris-HCl (pH 8), 5 mM EDTA, 8 M urea, and 2 mM β-mercaptoethanol at room temperature for at least 2 h. The soluble fraction was then injected onto a Q-Sepharose column equilibrated in 25 mM Tris-HCl (pH 8), 5 mM EDTA, and 5 M urea. The proteins were eluted in the flow-through and diluted two times before being refolded by dialysis into 250 mM Tris-HCl (pH 8.0), 100 mM L-Arg (for $V_L\kappa$ and λ variants) or 400 mM L-Arg (for V_H variants), 5 mM EDTA, 1 mM oxidized glutathione, and 0.5 mM reduced glutathione at 4 °C overnight. To remove misfolded aggregates and remaining impurities, the protein was cleaned using a Superdex 75 gel filtration column (GE Healthcare) equilibrated in PBS buffer. The recovery and purity of intact protein were verified by SDS-PAGE and matrix-assisted laser desorption/ionization time-of-flight mass spectrometry.

CD Measurements—CD measurements were performed using a Jasco J-720 spectropolarimeter (Jasco, Grossumstadt, Germany) equipped with a Peltier element. Far-UV CD spectra were measured using 10 μM protein in a 1-mm path length cuvette between 260 and 200 nm. Near-UV CD was measured between 320 and 250 nm using 50 μM protein in a 1-mm cuvette. All spectra were accumulated 16 times, and buffer was corrected. Thermal transitions were recorded using 10 μM protein at 212 nm for $V_L\kappa$ and 205 nm for $V_L\lambda$ and V_H variants with a heating and cooling rate of 20 °C/h.

Tryptophan Fluorescence Measurements—Unless otherwise stated, all fluorescence measurements were carried out using a FluoroMax-4 spectrofluorimeter (Horiba Jobin Yvon, Bensheim, Germany). Tryptophan fluorescence measurements were performed with excitation and emission slit widths of 2 and 3 nm, respectively. The protein concentration in a 1-cm quartz cuvette was 1 μM. The sample was excited at 280 nm, and spectra were recorded between 300 and 450 nm. Equilibrium unfolding and refolding transitions were carried out by denaturing 1 μM protein overnight at different concentrations of GdmCl (between 0 and 3 M GdmCl). Fluorescence intensity at 358 nm was measured for 50 s, and the average was taken. Analysis of data was carried out using the linear extrapolation method described previously (14, 19).

1-Anilino-8-naphthalene Sulfonate (ANS) Binding Assay—ANS binding was measured by fluorescence emission recorded from 400 to 650 nm, with excitation at 380 nm with excitation and emission slit widths of 2 and 3 nm, respectively. Experiments were performed at a protein concentration of 10 μM and an ANS concentration of 100 μM in 1-cm quartz cuvette. All spectra were accumulated three times and averaged.

Fibril Formation with Ultrasonication—For the standard reaction, the V_L variants were diluted at a concentration of 30 μM in PBS solution and 5 μM thioflavin T (ThT). Then 0.2 ml of the V_L variant solution was applied to each of the 96 wells of a microplate (Greiner Bio-One on a 96-well microplate 675-074 made of polystyrene with a size of 128 × 85 mm). The microplate was set on the HANABI (HANdai Amyloid Burst Inducer), which combines the use of a water bath-type ultrasonicator (ELESTEIN, Elekon, Chiba, Japan) and a microplate reader (SH-9000, Corona Electric Co., Ibaraki, Japan). The water bath with 400 × 250 mm × 230 nm (height) contains about 12 liters of water, and three ultrasonic transducers are set, two on the sides and one at the bottom. Pulses were applied to the microplate from three directions, focusing on the center position, for cycles of 1 min followed by a quiescent period of 9 min. The measurement temperature was maintained at 37 °C. The formation of fibrils was monitored by ThT fluorescence

with excitation and emission wavelengths of 450 and 490 nm, respectively. Microplates were incubated at 37 °C and shaken before the measurements. Transmission electron microscopy (TEM) images were taken using a HITACHI H-7650 transmission microscope, (Hitachi, Tokyo, Japan), with an acceleration voltage of 80 kV. Aliquots (5 μl) of the samples were placed on a 400-mesh copper grid covered by a carbon-coated colloidal film for 60 s. Two percent (w/v) uranyl acetate solution (5 μl) was then placed on the grid to stain the samples for 60 s. Excess sample solutions on the grid were removed with a filter paper. The magnification on the representative pictures was 30,000-fold.

Fibril Formation without Ultrasonication—Samples of V_L at a concentration of 30 μM in PBS buffer (pH 7.4), containing 0.05% sodium azide (or acetate buffer (pH 2)) were incubated with shaking (gentle agitation) in a roller shaker at 37 °C for at least 1 week. At various intervals, a 20-μl aliquot was withdrawn for ThT binding and TEM. For the ThT binding, 10 μl of protein aliquot was added to 480 μl of a PBS buffer (pH 7.4) followed by the addition of 10 μl of 500 μM ThT prepared in PBS buffer (pH 7.4) (ThT final concentration 10 μM). This was left to incubate for 90 s before acquiring the emitted signal in a 1-cm quartz cuvette from 430 to 570 nm with excitation at 440 nm. The spectra were recorded using an FP-6500 spectrofluorimeter (Jasco) equipped with a Jasco ADP-303T Peltier as temperature controller. The excitation and emission slit widths were both 3 nm. A scan speed of 100 nm/min, an integration time of 1 s, and a 0.5-nm recording interval were used. Three scans were averaged for each sample. Rayleigh (elastic) light scattering at an angle of 90° was also measured at the excitation wavelength peak of 440 nm (20, 21). Therefore, for the same sample, information on its light scattering ability (presence of macromolecular assemblies or aggregation) and ThT binding (fibril formation) was assessed. For comparison, the Rayleigh scattering intensity at 440 nm and the ThT fluorescence intensity at 480 nm were used.

For TEM measurements, a 10-μl protein aliquot was fixed on a 200-mesh activated copper grid and incubated for 60 s. After a washing step with 10 μl of H_2O, the samples were stained with 10 μl of a 1.5% uranyl acetate solution. Samples were recorded with an acceleration voltage of 100 kV at a magnification of ×33,000 on a transmission electron microscope JEM100CX (Jeol).

Thermally Induced Aggregation—Native MAK33 or 1OPG $V_L\kappa$ at a concentration of 10 μM in PBS buffer (pH 7.4) with 10 μM ThT was subjected to increasing temperatures from 20 to 80 °C in steps of 5 °C in a 1-cm path cuvette. After thermal equilibration for 3 min, emission spectra were recorded for Rayleigh scattering and ThT fluorescence (21) as stated under "Fibril Formation without Ultrasonication."

NMR Spectroscopy—All NMR spectra were recorded using uniformly ^{15}N,^{13}C-labeled proteins in 20 mM phosphate, 50 mM NaCl (pH 6.5) at 298 K. Backbone resonance assignments of MAK33 $V_L\kappa$-WT and MAK33 $V_L\kappa$-I2E were transferred from previous assignments of MAK33 $V_L\kappa$-S20N (data not shown). The assignment was accomplished based on three-dimensional HNCA, HNCACB, CBCACONH, HNCO, and HNCACO experiments (22). Experiments were carried out at 1 mM protein concentration. Those residues, for which the assignment could not be transferred from MAK33 $V_L\kappa$-S20N, were assigned based on an HNCA experiment using a 100 μM MAK33 $V_L\kappa$-I2E sample. All spectra were recorded on a Bruker AVANCE 900MHz spectrometer (Bruker Biospin) equipped with a triple-resonance cryoprobe. Spectra were processed using TOPSPIN 3.2 (Bruker BioSpin) and analyzed with CcpNmr 2.2.2 (23). For determination of residues affected by the I2E substitution, ^{15}N HSQC spectra of MAK33 $V_L\kappa$-WT and MAK33 $V_L\kappa$-I2E, both at 50 μM, were acquired on a Bruker Avance 600MHz spectrometer equipped with a cryoprobe. For all residues, chemical shift perturbations were determined using Equation 1,

$$\Delta\delta^{res} = \sqrt{(\Delta\delta^{1H})^2 + \frac{1}{25}\cdot(\Delta\delta^{15N})^2}$$

with $\Delta\delta^{res}$ being the weighted chemical shift difference, $\Delta\delta^{1H}$ as the chemical shift of the amide proton in ppm, and $\Delta\delta^{15N}$ as the chemical shift of the amide nitrogen in ppm.

For comparison of signal intensities, all signals, which displayed significant overlap in one of the proteins, were ignored. Intensities were normalized for both proteins to the same average intensity.

MD and Umbrella Sampling (US) Simulations—Start structures of MAK33 $V_L\kappa$ domains and $V_L\lambda$ and V_H domains were obtained by extracting the corresponding coordinates from the crystal structures 1FH5 (MAK33 $V_L\kappa$), 1OPG, 1AQK, and 1VGE. Residue 2 of MAK33 $V_L\kappa$, 1AQK $V_L\lambda$, 1VGE $V_L\kappa$, and 1VGE V_H was substituted *in silico* with Glu although residue 2 of 1OPG, and $V_L\kappa$ was replaced with Ile. *In silico* substitutions were performed using the SPDBV package (24), while selecting the best fitting side chain rotamer. All MD simulations and the analysis of root mean square deviations (r.m.s.d.) and fluctuations were performed using the Amber12 package (25). Proteins were solvated in octahedral boxes, including explicit ions and explicit (TIP3P) water molecules (26). The simulation systems were first energy-minimized (5000 steps) followed by heating up to 300 K in steps of 100 K with position restraints on all heavy atoms of the proteins. Subsequently, positional restraints were gradually removed from an initial 25 kcal mol^{-1} $Å^{-2}$ to 0.5 kcal mol^{-1} $Å^{-2}$ within 0.5 ns followed by a 1-ns unrestrained equilibration at 300 K. All production simulations were performed at a temperature of 300 K and a pressure of 1 bar. US simulations were performed using the distance between the Cα atom of residue 2 and the Cα of residue 32 at the floor of the binding region for residue 2 in the $V_L\kappa$ domains as a reaction coordinate. A quadratic penalty potential ($k\,(d_{C\alpha\text{-}C\alpha} - d_{ref})^2$, force constant k = 2.0 kcal mol^{-1} $Å^{-2}$) for the Cα-Cα distance was used with reference distances varying from 11.5 to 16 Å in 0.5-Å steps and from 16 to 20 Å in 1-Å steps. At ~12–13 Å, residue 2 stays bound to the protein in the cavity as observed in the experimental x-ray structure, whereas it adopts a fully exposed state at distances of >16 Å. The associated potential of mean force was calculated using the weighted histogram analysis method (27).

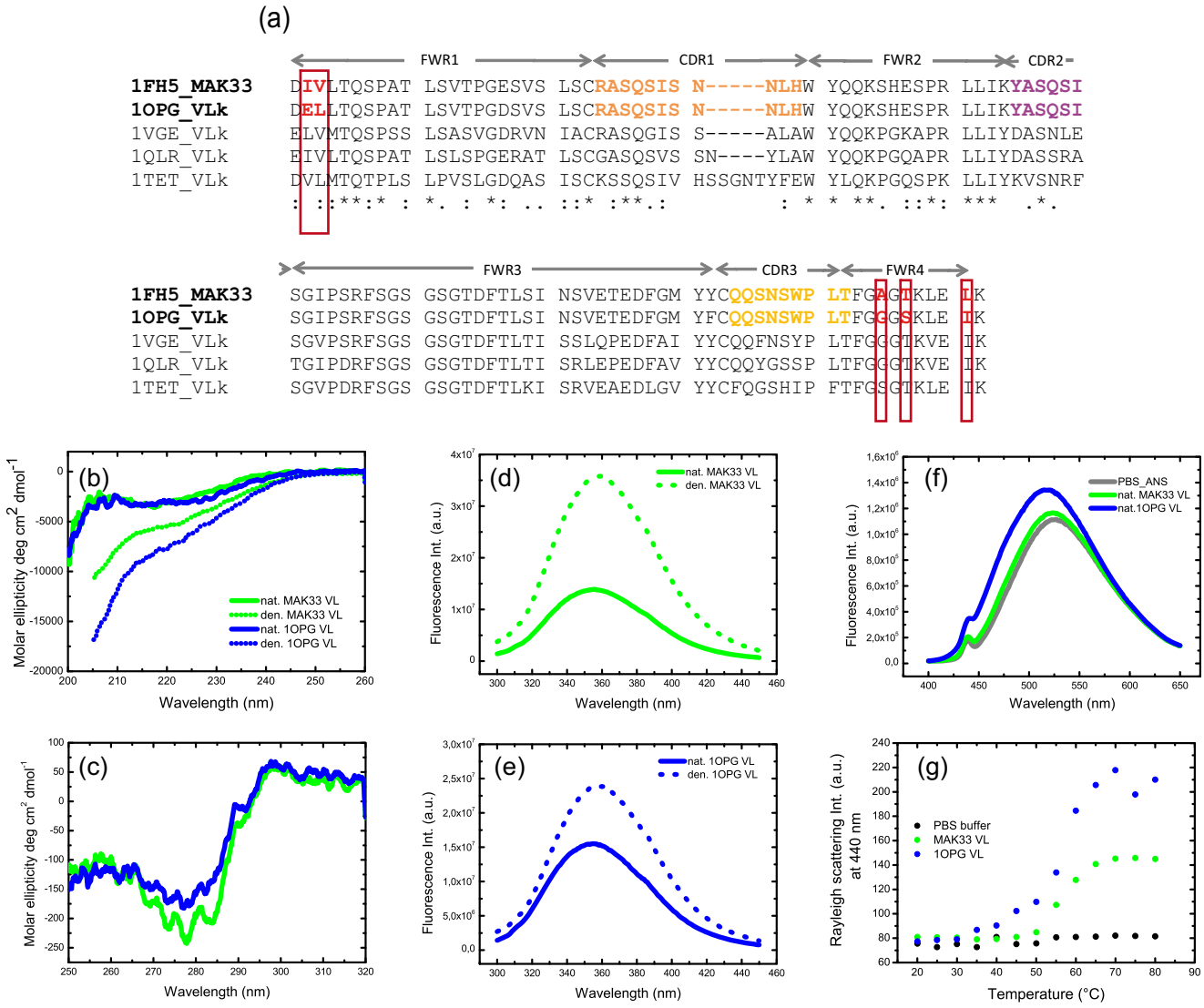

FIGURE 1. **Sequence analysis of $V_L\kappa$ domains, spectroscopic characterization of MAK33 $V_L\kappa$ and 1OPG $V_L\kappa$.** *a,* multiple sequence alignment of $V_L\kappa$ sequences. Five representative sequences are shown. MAK33 $V_L\kappa$ differs from 1VGE $V_L\kappa$ at 40 positions and from 1OPG $V_L\kappa$ at five positions as marked by *red rectangles*. Identical CDRs between MAK33 $V_L\kappa$ and 1OPG $V_L\kappa$ domains are highlighted in different colors. *b,* far-UV CD spectra of native (*continuous line*) and temperature-denatured (*dotted line*; 60 °C) MAK33 $V_L\kappa$ and 1OPG $V_L\kappa$ in PBS buffer. *c,* near-UV CD spectra of native MAK33 $V_L\kappa$ (*green line*) and 1OPG $V_L\kappa$ (*blue line*). Intrinsic tryptophan fluorescence spectra of native (*continuous line*) and 3 M GdmCl-denatured (*dotted lines*) MAK33 $V_L\kappa$ (*d*) and 1OPG $V_L\kappa$ (*e*) in PBS buffer. *f,* ANS fluorescence spectra of native MAK33 $V_L\kappa$ (*green line*) and 1OPG $V_L\kappa$ (*blue line*). The *gray line* is PBS/ANS without protein. *g,* thermally induced aggregation of MAK33 $V_L\kappa$ and 1OPG $V_L\kappa$ domains monitored by Rayleigh (elastic) light scattering at 440 nm.

RESULTS

Biophysical Characteristics, Stability, and Amyloidogenic Propensity of Two Highly Homologous $V_L\kappa$ Domains—MAK33 is a well studied IgG antibody with respect to folding and association. In this context, the folding pathway of the V_L domain has been analyzed in detail (15); its amino acid composition is typical for a murine κ/IgG1 light chain variable domain (PDB code 1FH5 (28)). Interestingly, another antibody $V_L\kappa$ domain exists (PDB code 1OPG (29)), which has identical CDRs but five differences in the framework region (Fig. 1*a*). We were wondering whether these differences affect the structural properties of the domain. Both isolated domains were expressed, purified, and characterized. The far-UV circular dichroism (CD) spectra of the $V_L\kappa$ domains were similar with a minimum at 218 nm (Fig. 1*b*) characteristic of the β-sheet conformation. However, the shapes of both native spectra suggest a large contribution of random coils, which might be due to long flexible CDR loops. Their near-UV CD spectra (Fig. 1*c*) with a minimum at 275 nm confirmed that the tertiary structure of both proteins is correctly formed (30, 31). The presence of a buried tryptophan in close proximity to the disulfide in antibody domains makes it a sensitive probe for studying conformational changes by fluorescence. Intrinsic tryptophan fluorescence spectra of both $V_L\kappa$ domains showed MAK33 $V_L\kappa$ to have a large (~2.5-fold) increase in fluorescence emission intensity (maximum at ~358 nm) in the presence of 3 M GdmCl (Fig. 1*d*), as opposed to a small increase observed in 1OPG $V_L\kappa$ (Fig. 1*e*). This suggests already a partial exposure of tryptophan in the native 1OPG $V_L\kappa$. To verify whether the $V_L\kappa$ domains exposed hydrophobic patches on their surfaces, ANS binding assay was performed. As depicted in Fig. 1*f*, 1OPG $V_L\kappa$ binds ANS with an increase and a blue-shifted fluorescence emission maximum (shift from 525

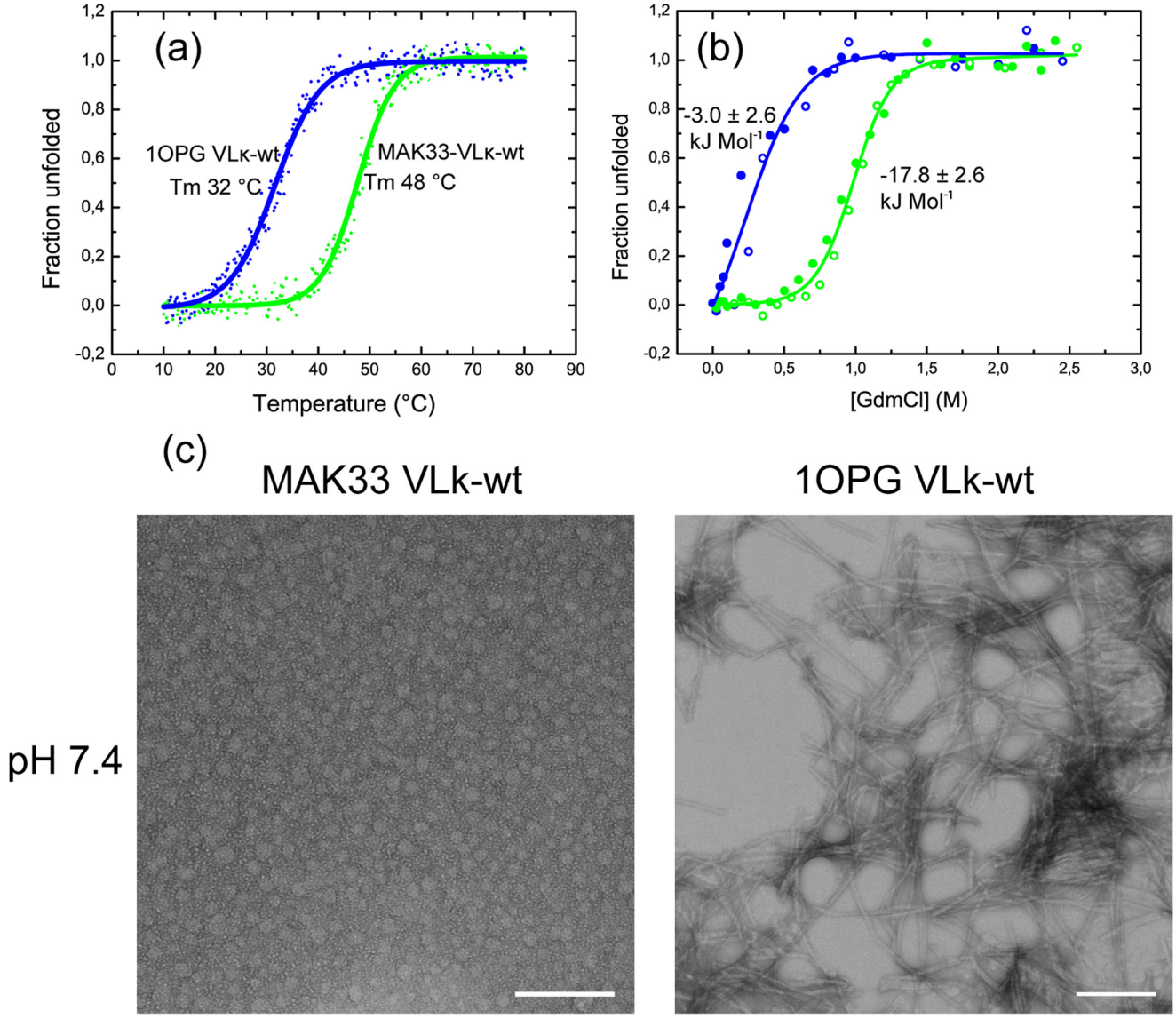

FIGURE 2. **Stability and amyloidogenic propensity of MAK33 $V_L\kappa$ and 1OPG $V_L\kappa$ domains.** *a,* thermal unfolding transitions of MAK33 $V_L\kappa$ (*green symbols*) and 1OPG $V_L\kappa$ (*blue symbols*). The *solid lines* indicate the theoretical curves derived by fitting the data to a Boltzmann function for MAK33 VLκ (*green*) and 1OPG $V_L\kappa$ (*blue*) to obtain transition midpoints (T_{melt}). *b,* GdmCl-induced unfolding transitions of MAK33 VLκ (*green*) and 1OPG $V_L\kappa$ (*blue*). The reversibility of the GdmCl-induced unfolding process is shown by the overlay of unfolding symbols (*open circles*) and refolding (*closed circles*) experiments. The *solid lines* show the fit to a two-state mechanism for both MAK33 $V_L\kappa$ (*green line*) and 1OPG $V_L\kappa$ (*blue line*) to obtain thermodynamic stability values (ΔG_U) and the cooperativity parameters (*m* values). *c,* transmission electron microscopy micrographs of MAK33 VLκ and 1OPG $V_L\kappa$ from amyloid induction experiments at neutral pH, 37 °C, and 1 week incubation with gentle agitation. *Scale bars,* 200 nm.

to 515 nm), suggesting the presence of exposed hydrophobic patches. MAK33 $V_L\kappa$ shows no ANS binding (Fig. 1*f*).

The propensity of both MAK33 and 1OPG $V_L\kappa$ domains to aggregate with increasing temperatures was monitored by recording Rayleigh (elastic) scattering of ThT fluorescence excitation (440 nm) light (Fig. 1*f*) (20, 21). Surprisingly, 1OPG $V_L\kappa$ already starts aggregating at ~35 °C, although MAK33 $V_L\kappa$ only starts transforming into aggregates at ~50 °C (a difference of ~15 °C). Maximum aggregation for both proteins occurred at ~65 °C. No ThT binding was observed for any of the proteins at the experimental temperature range of 20–80 °C (data not shown), which implies that the aggregates formed by thermal induction did not contain amyloid fibrils. When we determined their stabilities against temperature monitored by far UV CD, we found, interestingly, that the 1OPG $V_L\kappa$ is 16 °C less stable than MAK33 $V_L\kappa$ as judged from their transition midpoints (Fig. 2*b*), which correlates very well with thermal-induced aggregation monitored by light scattering at 440 nm. Thermally induced unfolding transitions were not reversible for any of the proteins. For equilibrium unfolding and refolding in the presence of GdmCl monitored by Trp fluorescence, the MAK33 $V_L\kappa$ with a cooperative sigmoidal transition had identical midpoints in both the unfolding and refolding directions (Fig. 2*c*). This sigmoidal transition was not observed for 1OPG $V_L\kappa$, for which a native baseline could not be obtained (Fig. 2*c*). The GdmCl-induced unfolding transitions were cooperative and reversible. Assuming two-state transitions, the data were fitted using linear extrapolation (14, 19) that yielded an intrinsic stability of -17.8 kJ mol^{-1} for MAK33 $V_L\kappa$ and -3.0 kJ mol^{-1} for 1OPG $V_L\kappa$ and *m* values of 18.0 ± 2.4 and 12.9 ± 5.3, respec-

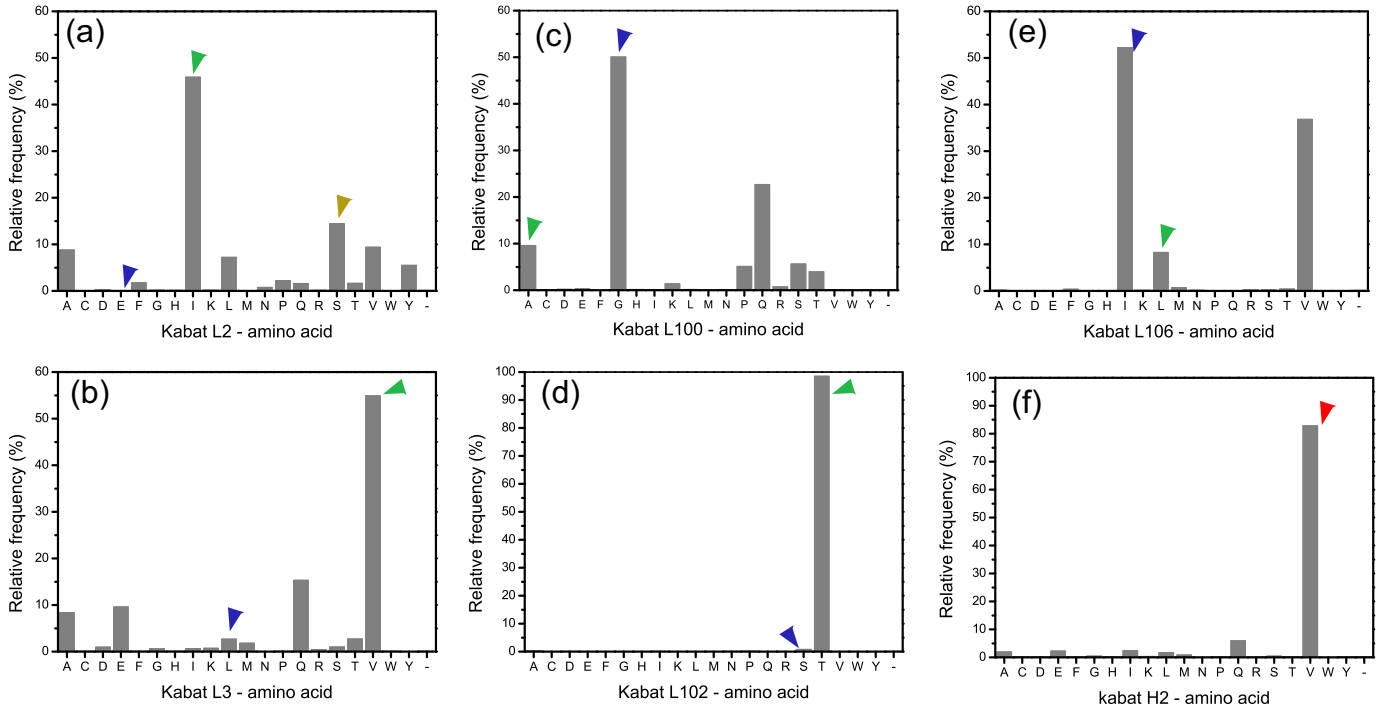

FIGURE 3. **Residue frequency distribution analysis at position 2 of variable domains and of the different positions between MAK33 $V_L\kappa$ and 1OPG $V_L\kappa$ domains.** Relative distribution of amino acid at various positions of light (*a–e*) and heavy chains (*f*). *Green arrowheads* indicate residue in MAK33 $V_L\kappa$, and the corresponding positions in 1OPG $V_L\kappa$ are shown by *blue arrowheads*. With the exception of positions 100 and 106, the residues found in MAK33 $V_L\kappa$ at positions 2, 3, and 102 are more frequent than those at corresponding positions in 1OPG $V_L\kappa$. The database could not separate λ LCs from the κ LCs during the distribution analysis. But an observation of most of the sequences show that Ser-2 is almost entirely contributed by the λ LCs (*orange arrowhead* in *a*). *f*, *red arrowheads* indicate the most frequent residue at position 2 of heavy chains. Sequences from all organisms were considered for the analysis. Analysis was based on the Kabat numbering scheme accessed through the antibody (abYsis database) (Dr. Andrew C. R. Martin's Group, University College London).

tively, which reflects the different cooperativities observed. Although the stability of MAK33 $V_L\kappa$ falls within the range of those reported for amyloidogenic V_L domains (~15–20 kJ mol^{-1}) (32, 33), it is known to be nonamyloidogenic *in vitro* at physiological pH (15). Accordingly, after 1 week of incubation in PBS buffer at pH 7.4 and 37 °C with gentle agitation, MAK33 $V_L\kappa$ did not form any amyloid fibrils (Fig. 2*c*). However, under these conditions, 1OPG $V_L\kappa$ readily turned into well defined fibrillar structures (Fig. 2*c*). When the proteins were incubated in an acidic buffer (pH 2) under similar conditions, fibrils were detected for both MAK33 $V_L\kappa$ and 1OPG $V_L\kappa$ samples (data not shown), confirming our previous results on MAK33 $V_L\kappa$ (15). This supports the notion that under appropriate destabilizing conditions, even proteins not known to form amyloid fibrils under normal physiological conditions can indeed fibrillize (34–36).

To assess how conserved the frameworks of both $V_L\kappa$ domains are in comparison with other $V_L\kappa$ sequences, a comprehensive sequence analysis was performed using the abYsis database, which integrates sequences from the Kabat (37) and IMGT (38) databases. Fig. 1*a* depicts five representative $V_L\kappa$ sequences from this alignment. Considering amino acid side chain chemistry, all framework residues are very similar, except for residue 2. In 1OPG $V_L\kappa$, this residue is a Glu, although in most other $V_L\kappa$ frameworks an aliphatic residue is found at the same position (Fig. 1*a*). A residue frequency distribution analysis using the abYsis database with all available (~20,000 nonidentical) LC sequences revealed that Ile occurs with the highest frequency (46%) at position 2 (Fig. 3). Other aliphatic residues like Val, Leu, and Ala represent 7–9% at this position in V_L domains and charged residues (Glu, Asp, Lys, and Arg) only <1% (Fig. 3*a*). In addition, looking at the residue frequency distribution at position 102 of these V_L domains, we observed a highly conserved Thr with a frequency of 98%, although all other residues had a <1% frequency of occurrence (Fig. 3*d*). In the more conformationally stable MAK33 $V_L\kappa$, position 102 is occupied by Thr, whereas in the less stable 1OPG $V_L\kappa$, the less frequent Ser is found. With positions 2 and 102 showing huge frequency distribution discrepancies between the two $V_L\kappa$ domains, we wondered whether these positions were responsible for the different behaviors of the two proteins. In consequence, we exchanged these residues between the two $V_L\kappa$ domains and monitored their effects on stability and amyloid fibril formation.

Residue 2 Is Crucial for the Stability of $V_L\kappa$ Domains—To identify residue(s) that predispose 1OPG $V_L\kappa$ for lower stability and fibril formation, single point variants were generated by replacing residues in 1OPG $V_L\kappa$ with corresponding residues of MAK33 $V_L\kappa$ at any of the five different positions (OP-E2I, OP-L3V, OP-G100A, OP-S102T, and OP-I106L). All five substitutions were correctly folded as revealed by UV CD spectra. The thermal unfolding of these variants showed a striking increase in thermal stability for OP-E2I with a T_{melt} value of 43.1 °C, compared with 31.6 °C for 1OPG $V_L\kappa$-WT. Also, OP-E2I was significantly more stable toward GdmCl than 1OPG $V_L\kappa$-WT (Fig. 4, *a* and *c*; Table 1). OP-S102T was only slightly more stable, and the other single point substitution variants were all similar to the less stable 1OPG $V_L\kappa$-WT (Table

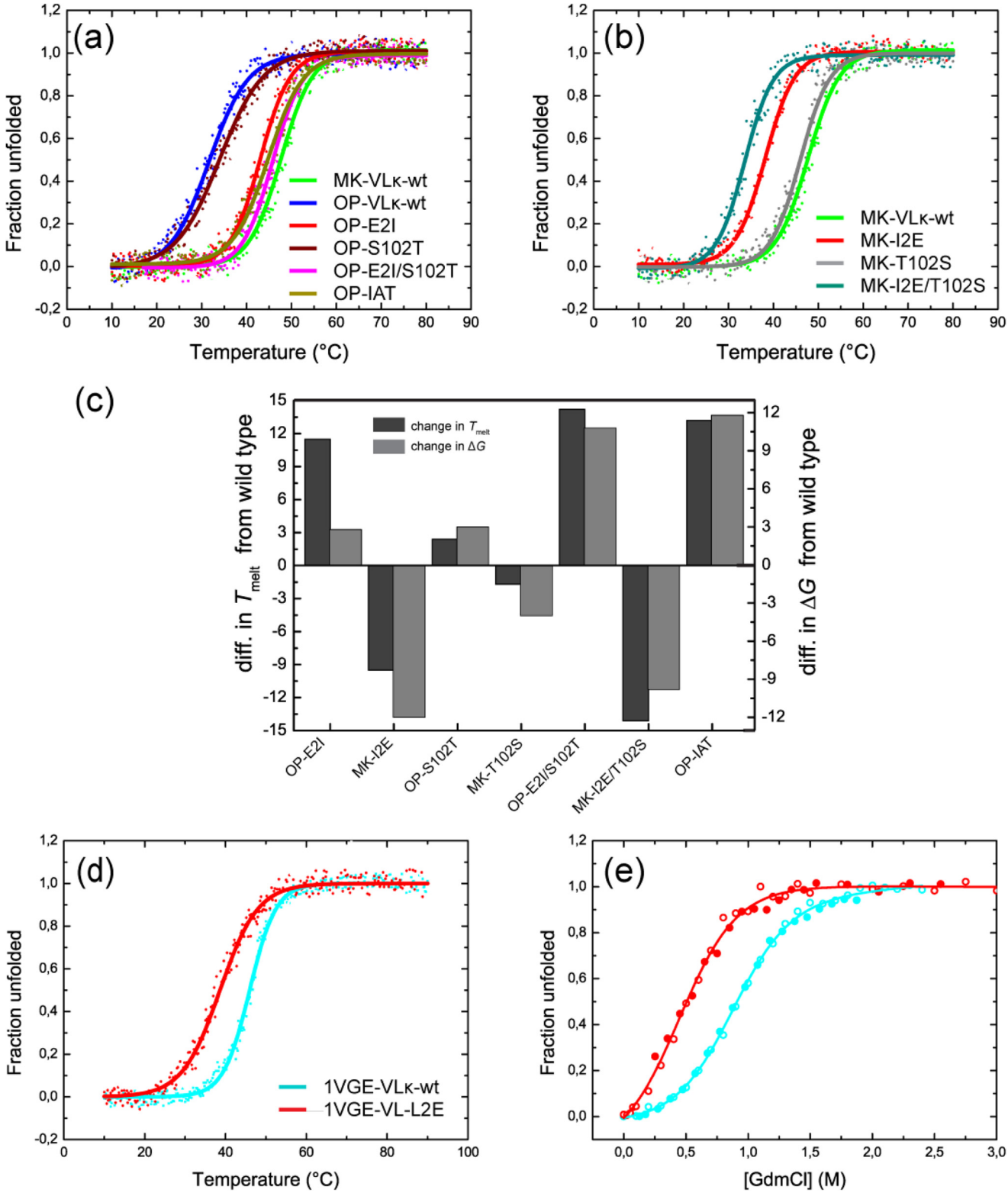

FIGURE 4. **Stability of the different $V_L\kappa$ variants.** Thermal unfolding transitions of 1OPG $V_L\kappa$ variants (*a*), MAK33 $V_L\kappa$ variants (*b*), and 1VGE $V_L\kappa$ variants (*d*). The *solid lines* indicate the theoretical curves derived by fitting the data to a Boltzmann function to obtain transition midpoints (T_{melt}). *c,* increase or decrease in stability caused by the different substitutions in 1OPG $V_L\kappa$ and MAK33 $V_L\kappa$, obtained by subtracting the T_{melt} and ΔG_U values of the wild type V_L from those of their corresponding mutants. *e,* GdmCl-induced unfolding transitions of 1VGE $V_L\kappa$ variants. The reversibility of the unfolding process is shown by the overlay of unfolding symbols (*open circles*) and refolding (*closed circles*) experiments. The *solid lines* show the fit to a two-state mechanism for $V_L\kappa$ variants to obtain thermodynamic stability values (ΔG_U) and the cooperativity parameters (*m* values).

TABLE 1

Thermal and chemical stabilities of 1OPG $V_L\kappa$ and MAK33 $V_L\kappa$ and 1VGE $V_L\kappa$ variants

Stabilities against the thermal and chemical (GdmCl) denaturation of different variants are shown. Midpoints of thermal transitions are shown as T_{melt}. Because the GdmCl-induced unfolding transitions were reversible, the data were fitted to a two-state equilibrium unfolding model to obtain the thermodynamic stability of unfolding (ΔG_U), as well as the cooperativity parameter (*m value*), for a qualitative comparison of the data.

Protein variant	T_{melt}	ΔG_U	*M* value
	°C	*kJ mol*$^{-1}$	*kJ mol*$^{-1}$ *M*$^{-1}$
1OPG $V_L\kappa$-WT	31.6 ± 0.2	−3.0 ± 2.6	12.9 ± 5.3
OP-E2I	43.1 ± 0.1	−5.8 ± 1.7	14.2 ± 1.7
OP-S102T	34.0 ± 0.2	−6.0 ± 1.6	16.6 ± 3.3
OP-E2I/S102T	45.8 ± 0.2	−13.8 ± 3.9	18.1 ± 4.4
OP-E2I/G100A/S102T	44.8 ± 0.4	−14.8 ± 4.0	16.4 ± 4.0
MAK33 $V_L\kappa$-WT	47.7 ± 0.2	−17.8 ± 2.6	18.0 ± 2.4
MK-I2E	38.2 ± 0.1	−5.8 ± 1.6	15.0 ± 3.0
MK-T102S	46.0 ± 0.2	−13.8 ± 3.1	18.2 ± 3.2
MK -I2E/T102S	33.6 ± 0.2	−8.0 ± 3.0	19.8 ± 2.3
MK-ΔD1	48.2 ± 0.2	−14.2 ± 3.7	13.5 ± 3.3
MK-ΔD1/I2	41.7 ± 0.1	−9.7 ± 1.7	15.6 ± 2.5
1VGE $V_L\kappa$-WT	46.0 ± 0.1	−.3 ± 0.4	10.7 ± 0.5
1VGE V_L-L2E	38.6 ± 0.2	−4.8 ± 0.6	10.7 ± 1.0

1), implying that the exchange of these residues is not important for the conformational stability of the domain. With the high increase in stability seen in OP-E2I and the small increase observed in OP-S102T, we next tested whether a combination of both substitutions (OP-E2I/S102T) and a triple substitution OP-E2I/G100A/S102T (OP-IAT) would further lead to increased stability. The double and triple substitution variants both unfolded with a T_{melt} of about 45 °C quite similar to that obtained for OP-E2I (Table 1), confirming only a small influence of the G100A and S102T substitutions on the thermal stability of the protein. However, in terms of stability to GdmCl, both variants were more stable than the respective single substitution variants (Fig. 4*c*; Table 1). These stability values observed for the double and triple substitution variants of 1OPG $V_L\kappa$ are similar to that of MAK33 $V_L\kappa$ wild type (Table 1). This demonstrates an additive effect of exchanges at different positions.

Because Glu-2 and Ser-102 to a minor extent were determined to be the destabilizing residues in 1OPG $V_L\kappa$, we were also interested in how they affect MAK33 $V_L\kappa$. Interestingly, MK-I2E was destabilized, whereas MK-T102S had stability values similar to that of MAK33 $V_L\kappa$-WT (Fig. 4, *b* and *c*; Table 1). Specifically, MK-I2E was ~10 °C less stable with a free energy of ~12 kJ mol^{-1} less than that of MAK33 $V_L\kappa$-WT. The combined substitution variant (MK-I2E/T102S) was less stable than both single substitution variants with a T_{melt} of 33.6 °C and a chemical stability of −8.0 kJ mol^{-} (Fig. 4*c*; Table 1). This again emphasizes the additive effect of both positions. To demonstrate that our findings on the pivotal role of residue 2 are general to the $V_L\kappa$ family, we investigated a human κ/IgG1 antibody V_L domain (1VGE $V_L\kappa$) (39), which differs greatly in amino acid sequence from 1OPG and MAK33 $V_L\kappa$. The N-terminal motif is ELV as opposed to DIV in MAK33 and DEL in 1OPG $V_L\kappa$ (Fig. 1*a*). To assess the role of residue 2 in this human $V_L\kappa$, Leu was replaced with Glu (1VGE V_L-L2E). Notably, analysis of their thermal and thermodynamic stabilities also revealed a decrease in thermal stability of ~10 °C and a 2-fold decrease in thermodynamic stability for 1VGE V_L-L2E compared with the wild type (Fig. 4, *d* and *e*; Table 1). This correlates very well with results obtained for MAK33 and 1OPG $V_L\kappa$, implying that the effects mediated by residue 2 are conserved within the $V_L\kappa$ family.

Influence of Sequence Variation on Amyloid Fibril Formation—To examine whether the increase in the stability of 1OPG $V_L\kappa$ variants also correlates with the resistance to amyloid formation, we set up ultrasonication amyloid induction assays at neutral pH at 37 °C (40–45). ThT fluorescence was used to monitor the fibrillation process (46, 47). All variants that had a thermodynamic stability of <10.0 kJ mol^{-1} (Table 1) bound ThT as indicated by an increase in fluorescence after a lag time of several hours, whereas the more stable variants (OP-E2I/S102T, OP-IAT, MAK33 $V_L\kappa$-WT, and MK-T102S) showed no ThT fluorescence (Fig. 5, *a* and *b*). The large fluctuations in ThT fluorescence amplitude are likely due to differences in higher order structure of amyloid fibrils as ThT fluorescence can change depending on the morphology of amyloid fibrils (41–43, 48). These variations in ThT fluorescence amplitudes might also depend on the mutants, and it is worth noting that ThT fluorescence is not always proportional to the amount of amyloid fibrils (48).

To confirm the presence of fibrils, transmission electron microscopy was performed. As expected, amyloid fibrils were detected in all variants for which ThT fluorescence was observed (Fig. 5*c*). Similar results were obtained with gentle agitation without ultrasonication after 4 or 10 days of incubation of the $V_L\kappa$ variants (data not shown). However, although the stable variants were protected from amyloid fibril formation, they did transform into amorphous aggregates upon prolonged incubation at 37 °C, revealed by the increase in Rayleigh scattering intensity (data not shown) Thus, the changes in V_L domain stability induced by modulating residue 2 inversely correlated with its ability to form amyloid fibrils.

Residue 2 Is a Decisive Factor for $V_L\kappa$ Domain Architecture—Alignment of $V_L\kappa$ sequences revealed a highly conserved N terminus for this family, with residue 1 always being an acidic residue (Asp or Glu) and residue 2 mostly an aliphatic residue (Ile, Leu, or Val) (Fig. 1*a*). We wondered whether the conserved residue 1 also affects the stability of $V_L\kappa$. Thus, N-terminal truncation variants of MAK33 $V_L\kappa$ were generated in which either the first residue (Asp-1) was deleted (MK-V_LΔD1) or one in which both the first (Asp-1) and the second (Ile-2) residues were truncated (MK-V_LΔD1/I2). Deletion of these N-terminal residues did not influence the structure of the domain as determined by CD spectroscopy. Surprisingly, the deletion of Asp-1 (MK-V_LΔD1) did not lead to changes in the thermodynamic stability when compared with the wild type domain. In contrast, the deletion of both Asp-1 and Ile-2 (MK-V_LΔD1/I2) resulted in a decrease in T_{melt} and thermodynamic stability of ~7 °C and ~10 kJ mol^{-1}, respectively (Fig. 6, *a* and *b*; Table 1), which is similar to the stability obtained by substituting Ile-2 alone with Glu (MK-I2E). These results show that residue 2 and not residue 1 is important for the stability of $V_L\kappa$ domains.

With Glu at position 2 identified to be destabilizing and Ile or Leu at the same position are stabilizing, we were interested to determine how residues with other side chains might affect the stability of these $V_L\kappa$ domains. Considering the residue frequency distribution at position 2 of V_L (Fig. 3*a*), residue 2 of

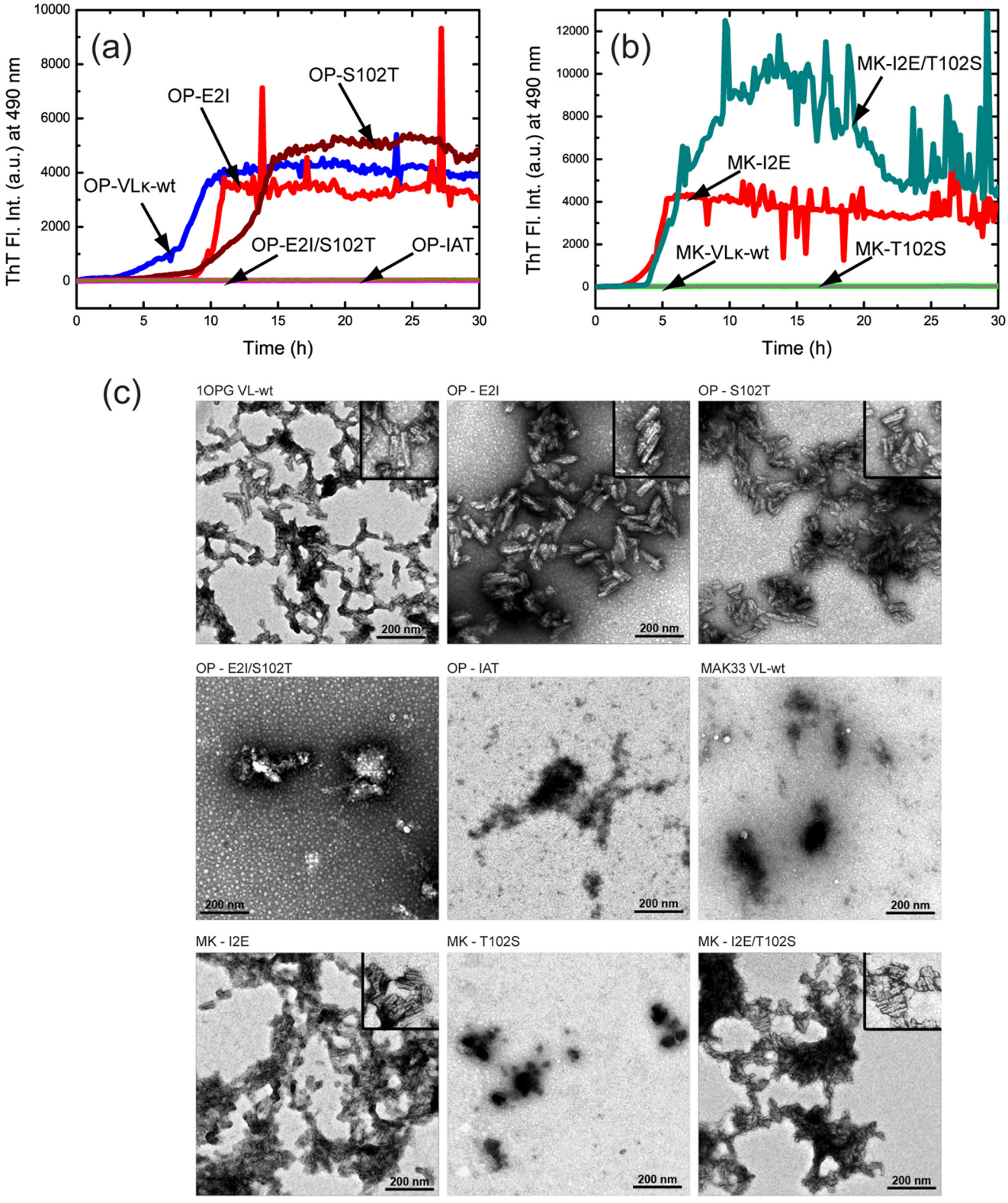

FIGURE 5. **Amyloidogenicity of $V_L\kappa$ variants.** 30 μM of each $V_L\kappa$ variant in a PBS buffer at pH 7.4 in the presence of ThT was subjected to ultrasonic pulses at 37 °C ($n = 3$). ThT fluorescence was monitored over time for 1OPG $V_L\kappa$ variants (*a*) and MAK33 $V_L\kappa$ variants (*b*), and TEM micrographs (*c*) were acquired at the end of the assay to detect the presence of fibrils. Variants with higher thermodynamic stabilities (>10 kJ mol^{-1}), OP-E2I/S102T and OP-IAT in *a* and MK-$V_L\kappa$-WT and MK-T102S in *b*, did not bind ThT, and as a result the curves of both proteins are superimposed.

1OPG $V_L\kappa$-WT and MAK33 $V_L\kappa$-WT were replaced with Ala, Leu, Asp, Lys, or Gln. Interestingly, the thermal unfolding transitions of these variants revealed striking differences. All variants with an uncharged residue at position 2 had a high thermal stability (Table 2). Although the respective 1OPG $V_L\kappa$ variants showed an increase in T_{melt} of 4–12 °C compared with their

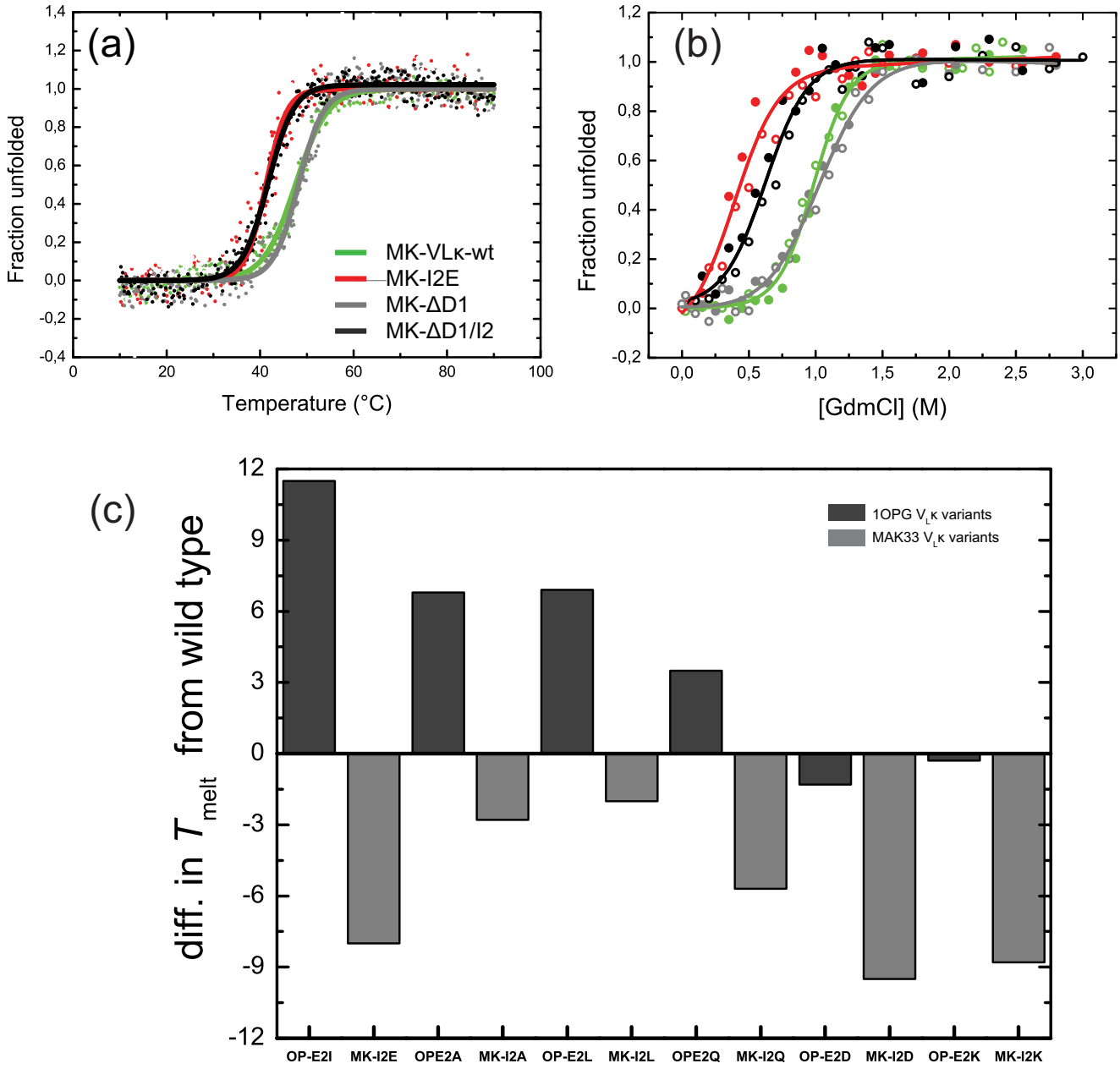

FIGURE 6. **Stability of the different MAK33 V_Lκ N-terminal variants and the different position mutants.** *a*, thermal unfolding transitions of MAK33 V_Lκ N-terminal variants. The *solid lines* indicate the theoretical curves derived by fitting the data to a Boltzmann function to obtain transition midpoints (T_{melt}). *b*, GdmCl-induced unfolding transitions of MAK33 V_Lκ N-terminal variants. The reversibility of the unfolding process is shown by the overlay of unfolding symbols (*open circles*) and refolding (*closed circles*) experiments. The *solid lines* show the fit to a two-state mechanism for V_Lκ variants to obtain thermodynamic stability values (ΔG_U) and the cooperativity parameters (*m* values), for a qualitative comparison of the data. *c*, increase or decrease in stability caused by different amino acid substitutions at position 2 of 1OPG V_Lκ and MAK33 V_Lκ, obtained by subtracting the T_{melt} value of the wild type V_L from those of their corresponding mutants.

TABLE 2

Thermal stabilities of various substitutions of residue 2 of 1OPG V_Lκ and MAK33 V_Lκ variants

Stabilities against thermal denaturation of the different 1OPG V_Lκ and MAK33 V_Lκ residue two variants are shown. Midpoints of the thermal transitions are shown as T_{melt}.

1OPG V_Lκ variant	T_{melt}	MAK 33 V_Lκ variant	T_{melt}
	℃		℃
1OPG V_Lκ-wt	31.6 ± 0.2	MAK33 V_Lκ-WT	52.0 ± 0.5
OP-E2I	43.1 ± 0.1	MK-I2E	44.0 ± 0.4
OP-E2A	38.4 ± 0.2	MK-I2A	49.2 ± 0.4
OP-E2L	38.5 ± 0.2	MK-I2L	50.0 ± 0.5
OP-E2Q	35.1 ± 0.2	MK-I2Q	46.3 ± 0.4
OP-E2D	30.3 ± 0.6	MK-I2D	42.5 ± 0.4
OP-E2K	31.3 ± 0.4	MK-I2K	43.4 ± 0.5

wild type, MAK33 V_Lκ variants with the same uncharged residues at position 2 had T_{melt} values similar to the more stable MAK33 V_Lκ-WT (Fig. 6*e*; Table 2). However, all variants with a charged residue (whether positive or negative) at position 2 were strongly destabilized. OP-E2D and OP-E2K were as unstable as 1OPG V_Lκ-WT, whereas the same substitutions in MAK33 V_Lκ resulted in an ~10 °C decrease in T_{melt} (Fig. 6*e*; Table 2).

Residue 2 Does Not Affect the Stability of V_Lλ and V_H Domains—Irrespective of the family, variable domains (V_Lκ, V_Lλ, and V_H) share a very similar topology of variable CDRs and

(a)

```
1AQK_VLλ    ENVLTQPPSV SGAPGQRVTI SCTGSNSNIG AGFTVHWYQH LPGTAPKLLI FANTNRPSGV
1NGP_VLλ    QAVVTQESAL TTSPGETVTL TCRSSTGAVT TSNYANWVQE KPDHLFTGLI GGTNNRAPGV
2FB4_VLλ    QSVLTQPPSA SGTPGQRVTI SCSGTSSNIG S-STVNWYQQ LPGMAPKLLI YRDAMRPSGV
4BJL_VLλ    ESVLTQPPSA SGTPGQRVTI SCSGSSSNIG E-NSVTWYQH LSGTAPKLLI YEDNSRASGV
1MCS_VLλ    PSALTQPPSA SGSLGQSVTI SCTGTSSDVG GYNYVSWYQQ HAGKAPKVII YEVNKRPSGV
```

(b)

```
1VGE_VH     QVKLLEQSGA EVKKPGASVK VSCKASGYSF TSYGLHWVRQ APGQRLEWMG WISAGTGNTK
1OPG_VH     EVQLVQSGG GLVNPGRSLK LSCAASGFTF SSYGMSWVRQ TPEKRLEWVA AISGGGTYIH
1AQK_VH     EVQLVESGG GVVQPGRSLR LSCAASGFTF NNYAIHWVRQ APGKGLEWVA FISYDGSKNY
1TET_VH     QIQLVQSGP ELKTPGETVR ISCKASGYTF TTYGMSWVKQ TPGKGFKWMG WINTYSGVPT
7FAB_VH     AVQLEQSGP GLVRPSQTLS LTCTVSGTSF DDYYWTWVRQ PPGRGLEWIG YVFYTG-TTL
```

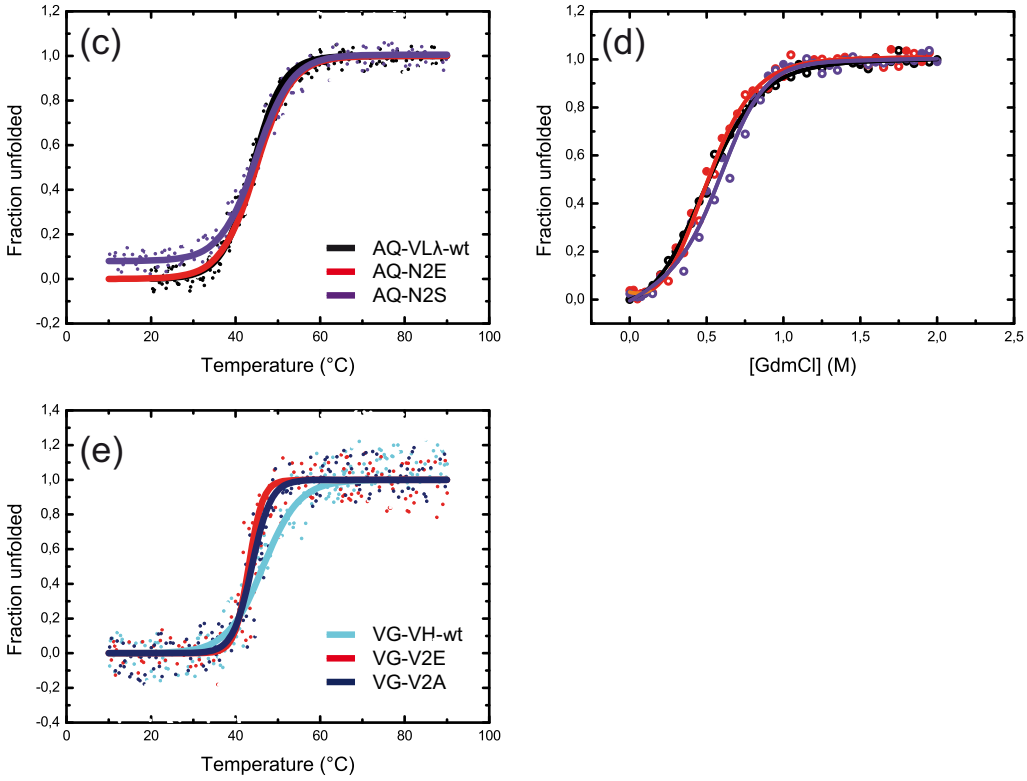

FIGURE 7. Multiple sequence alignment of $V_L\lambda$ (*a*) and V_H (*b*) domains is irrespective of organism. Five representative sequences are shown. Only the first 60 residues are presented. All sequences have a less diverse framework within each family. The N terminus of $V_L\lambda$ is mostly a QAV, ESV, or PSV motif with Ser the most frequent at position 2. In V_H, the N terminus is mostly an EVQ, AVQ, or QVK motif with Val the most frequent residue at position 2. Stability of 1AQK $V_L\lambda$ and 1VGE V_H variants; thermal unfolding transitions of the different 1AQK $V_L\lambda$ (*c*) and 1VGE V_H variants (*e*). The *solid lines* indicate the theoretical curves derived by fitting the data to a Boltzmann function to obtain transition midpoints (T_{melt}). *d,* GdmCl-induced unfolding transitions of 1AQK $V_L\lambda$ variants monitored by tryptophan fluorescence. The reversibility of the unfolding process is shown by the overlay of unfolding symbols (*open circles*) and refolding (*closed circles*) experiments. The *solid lines* show the fit to a two-state mechanism for all 1AQK $V_L\lambda$ variants to obtain thermodynamic stability values (ΔG_U) and the cooperativity parameters (*m* values). GdmCl-induced unfolding transitions of 1VGE V_H variants could not be performed due to less protein amounts.

a conserved framework. We were interested to determine whether residue 2 also plays a similar role in the λV_L and in the V_H domains. A multiple sequence alignment (Fig. 7, *a* and *b*) and a residue frequency distribution analysis at position 2 of $V_L\lambda$ and V_H showed this position in $V_L\lambda$ to be mostly occupied by Ser or Ala (Fig. 3*a*), although at the same position in V_H domains, Val occurs with a frequency of 83% (Fig. 3*f*). To ascertain the effects of residue 2 in these variable domains, a human λ/IgG $V_L\lambda$ (1AQK (49)) and a human IgG1 V_H (1VGE (39)) were examined. In the 1AQK $V_L\lambda$ domain, residue 2 (Asn-2) was replaced with either a Glu (1AQK $V_L\lambda$-N2E) or Ser (1AQK $V_L\lambda$-N2S). Unexpectedly, stability studies did not reveal any differences between the wild type and the 1AQK $V_L\lambda$-N2E mutant (Fig. 7, *c* and *d*; Table 3). This suggests that the stabiliz-

ing effects of residue 2 seen in the $V_L\kappa$ family cannot be ascribed to the $V_L\lambda$ family. Moreover, the mutant that contained Ser at position 2 (1AQK $V_L\lambda$-N2S) was slightly more stable than the wild type and 1AQK $V_L\lambda$-N2E mutant. When Val-2 of 1VGE V_H was substituted with a Glu (1VGE V_H-V2E) or Ala (1VGE V_H-V2A), again no pronounced thermal stability differences were observed (Fig. 7*e*; Table 3). Both 1VGE V_H-V2E and 1VGE V_H-V2A mutants were ~3 °C less stable than the wild type. Unlike in the $V_L\kappa$ family, the effects of residue 2 seen in V_H are minor and not specific for any amino acid side chain tested.

TABLE 3

Thermal and chemical stabilities of 1AQK $V_L\lambda$ and 1VGE V_H variants

Stabilities against thermal and chemical (GdmCl) denaturation of the different 1AQK $V_L\lambda$ and 1VGE V_H variants are shown. Midpoints of thermal transitions are shown as T_{melt}. Because GdmCl-induced unfolding transitions acquired for 1AQK $V_L\lambda$ were reversible, the data were fitted to a two-state equilibrium unfolding model to obtain the thermodynamic stability of unfolding (ΔG_U), as well as the cooperativity parameter (*m* value), for a qualitative comparison of the data. When due to too less an amount of proteins, the chemical stability experiments could not be performed (NA).

Variable domain variant	T_{melt}	ΔG	*M* value
	°C	kJ mol^{-1}	kJ mol^{-1} M^{-1}
1AQK $V_L\lambda$-WT	44.0 ± 0.2	−5.7 ± 1.3	13.1 ± 1.1
AQ-N2E	44.9 ± 0.5	−6.4 ± 1.7	15.1 ± 1.9
AQ-N2S	44.9 ± 0.4	−11.1 ± 3.0	17.8 ± 3.6
1VGE-V_H-WT	46.5 ± 0.6	NA	NA
VG-V2E	43.1 ± 0.6	NA	NA
VG-V2A	43.8 ± 0.5	NA	NA

Influence of Residue 2 on Domain Structure and Dynamics—To obtain a structural understanding of the influence of the residue at position 2 of $V_L\kappa$, both MAK33 $V_L\kappa$-WT and MAK33 $V_L\kappa$-I2E were analyzed by solution-state NMR spectroscopy. 71% of the non-proline residues could be assigned (Fig. 8*a*). Backbone assignment was hampered by chemical exchange dynamics. The unassigned residues mainly include the regions from the N terminus to Pro-8, from His-41 to Tyr-50, and from Cys-88 to Gly-101. Fig. 8*b* depicts chemical shift changes caused by the I2E substitution. We find particularly large chemical shift differences for residues Cys-23 to Ser-40

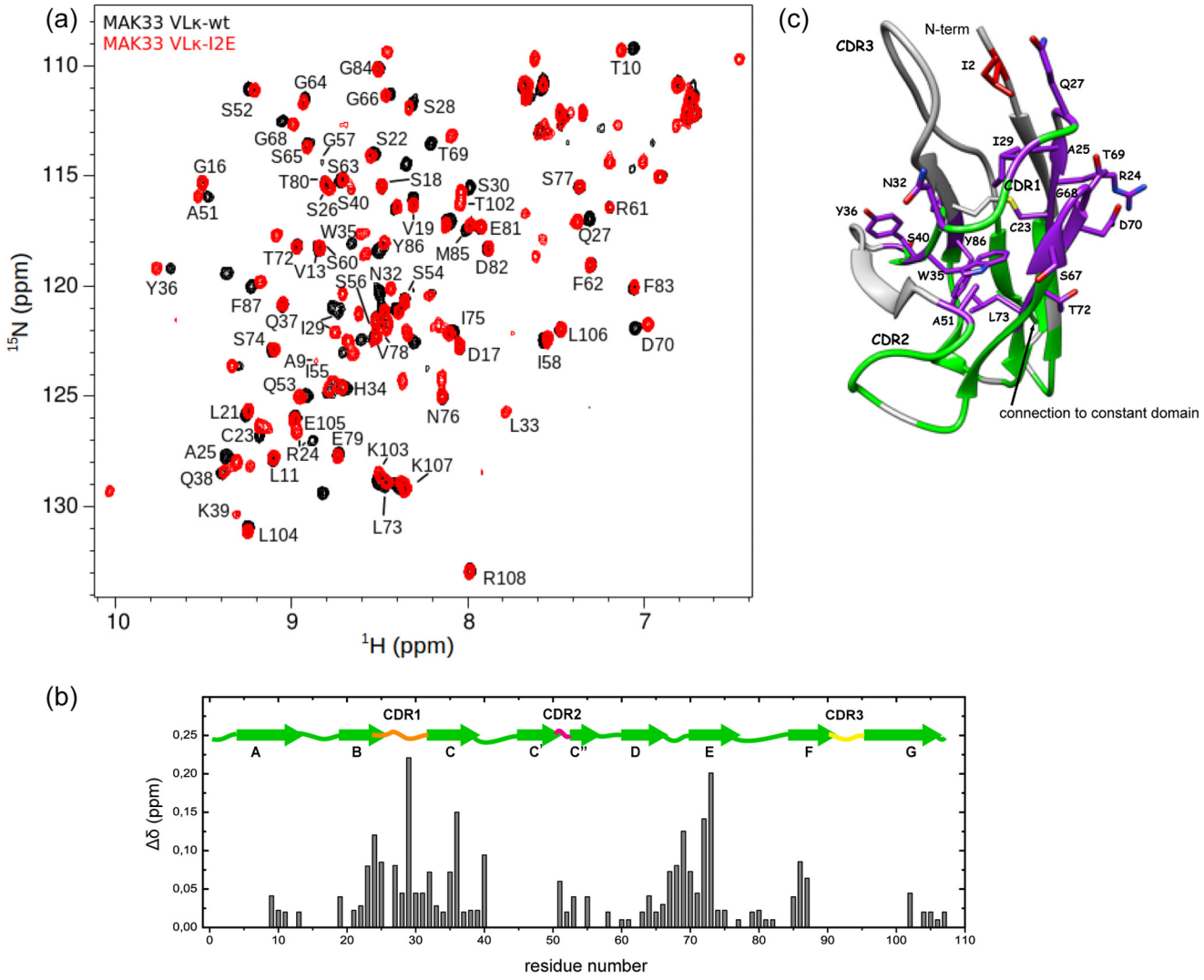

FIGURE 8. **Structural properties of V_L variants monitored by NMR spectroscopy.** *a*, ^{1}H-^{15}N-HSQC spectra of MAK33 $V_L\kappa$-WT and MAK33 $V_L\kappa$-I2E. Both spectra were acquired at a protein concentration of 50 μM in 20 mM phosphate, 50 mM NaCl (pH 6.5) at 298 K on a 600 MHz spectrometer equipped with a cryoprobe. *b*, chemical shift changes of MAK33 $V_L\kappa$ caused by the I2E substitution. ^{1}H and ^{15}N backbone chemical shifts were determined at a protein concentration of 50 μM at 298 K in 20 mM phosphate, 50 mM NaCl (pH 6.5). *c*, effects of I2E substitution in MAK33 $V_L\kappa$. Strongly affected residues are marked on the MAK33 VLκ-WT crystal structure (PDB code 1FH5). Ile-2 is shown in *red*, and residues with chemical shift changes >0.05 ppm are shown in *dark purple*, and unassigned residues are shown in *gray*.

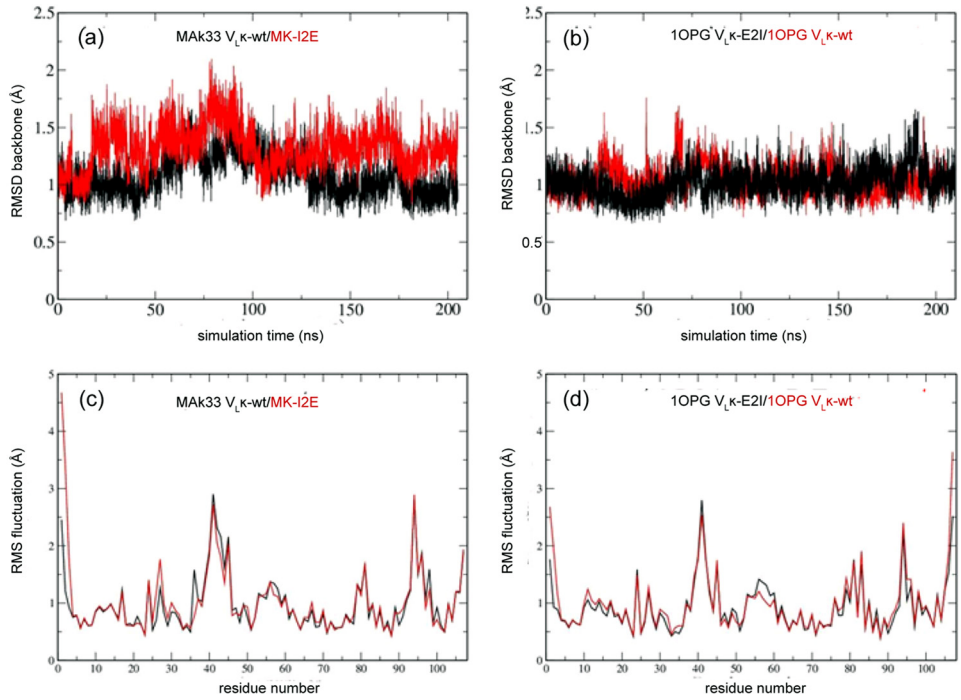

FIGURE 9. *a,* comparison of backbone root mean square deviations (*RMSD*) from the corresponding experimental start structure *versus* data gathering simulation time for MAK33 $V_L\kappa$-WT (*black curve*) and MAK33 $V_L\kappa$-I2E (*red curve*). *b,* same for 1OPG $V_L\kappa$-WT (*red curve*) and 1OPG $V_L\kappa$-E2I (*black curve*). *c,* comparison of root mean square fluctuations of amino acid residues along the domain chain for 200-ns simulations of MAK33 VLκ-WT (*black curve*) and MAK33 VLκ-I2E (*red curve*). *d,* same for 1OPG $V_L\kappa$-WT (*red curve*) and 1OPG $V_L\kappa$-E2I (*black curve*).

and Ser-67 to Leu-73. The first region contains the structurally important residues Cys-23, which forms a conserved disulfide bond with Cys-88. The adjacent Arg-24 is involved in a conserved salt bridge with Asp-70 and the conserved Trp-35 lies in the core of Ig domains (50). Furthermore, the I2E substitution causes structural changes also at distant residues like Tyr-86 and Phe-87 (Fig. 8*c*). In consequence, a rearrangement of the hydrophobic core involving residues Ala-25, Ile-29, Trp-35, Leu-73, and Tyr-86, which exhibit major chemical shifts changes, is induced. The CDRs also show shift perturbations, especially the loop including residues Arg-24 to Ile-29, which is close to the N terminus.

To gain further insight in the dynamics of the $V_L\kappa$ domains, MD simulations in explicit solvent were performed on the MAK33 $V_L\kappa$-WT and 1OPG $V_L\kappa$-WT domains and on the MAK33 $V_L\kappa$-I2E and 1OPG $V_L\kappa$-E2I mutants. The substitutions were generated *in silico* based on the native crystal structures followed by extensive energy minimization before starting MD simulations (see "Experimental Procedures" for details). For all four cases, the r.m.s.d. of the backbone stayed close to the starting structure within <2.0 Å (Fig. 9). In the variants with an Ile at position 2 (MAK33 $V_L\kappa$-WT and 1OPG $V_L\kappa$-E2I), the Ile residue remained close to the starting conformation with the side chain located in a hydrophobic cavity (Fig. 10, *a*, *b*, and *d*). During the entire simulation, the r.m.s.d. of the heavy atoms of Ile-2 stayed at a level similar or only slightly larger than that of the average backbone r.m.s.d. of the complete domains (*black curves* in Fig. 10, *a* and *b*). Interestingly, one can distinguish two rotameric sub-states of the Ile side chain during the simulation with slightly different r.m.s.d. with respect to the starting structure. Contrary to this, in the two variants with a Glu at position 2 (MAK33 $V_L\kappa$-I2E and 1OPG $V_L\kappa$-WT), significant deviations and fluctuations of the Glu-2 side chains with respect to the starting structure were observed (*red curves* in Fig. 10, *a* and *b*). Deviations of up to 6–8 Å from the initial placement were observed that correspond to a partial or full dissociation of the Glu-2 side chain from the cavity, thereby adopting a fully solvent-exposed conformation (compare Fig. 10, *d* and *e*). The frequent disruption of contacts between Glu-2 and other side chains indicates that Glu does not contribute significantly to the stability.

The analysis of root mean square fluctuations of each residue with respect to the mean structure (Fig. 9, *c* and *d*) showed similar fluctuations for wild type and corresponding mutant chains. However, significantly larger fluctuations were observed for variants with a Glu at position 2 compared with those with Ile-2. Slightly increased fluctuations were also seen at loop segments that flank residue 2 (*e.g.* the loop around Ala-25), also identified in NMR experiments to have strong chemical shift perturbations. To quantify the relative stability of solvent-exposed and buried states of the side chain at residue 2, US simulations were performed to induce a dissociation of the side chain from the N-terminal cavity region. The distance between the Cα atom of residue 2 and the Cα atom of a residue at the floor of the N-terminal contact region served as reaction coordinate (see "Experimental Procedures" for details). The US simulations allowed for the calculation of a potential-of-mean force or associated free energy change for the dissociation of residue 2 (Fig. 10*c*). A distance of ~12 Å corresponded to a location of residue 2 in contact with the residues forming the N-terminal cavity region (smaller distances resulting in sterical repulsion). At distances of 16–18 Å, the side chain of residue 2

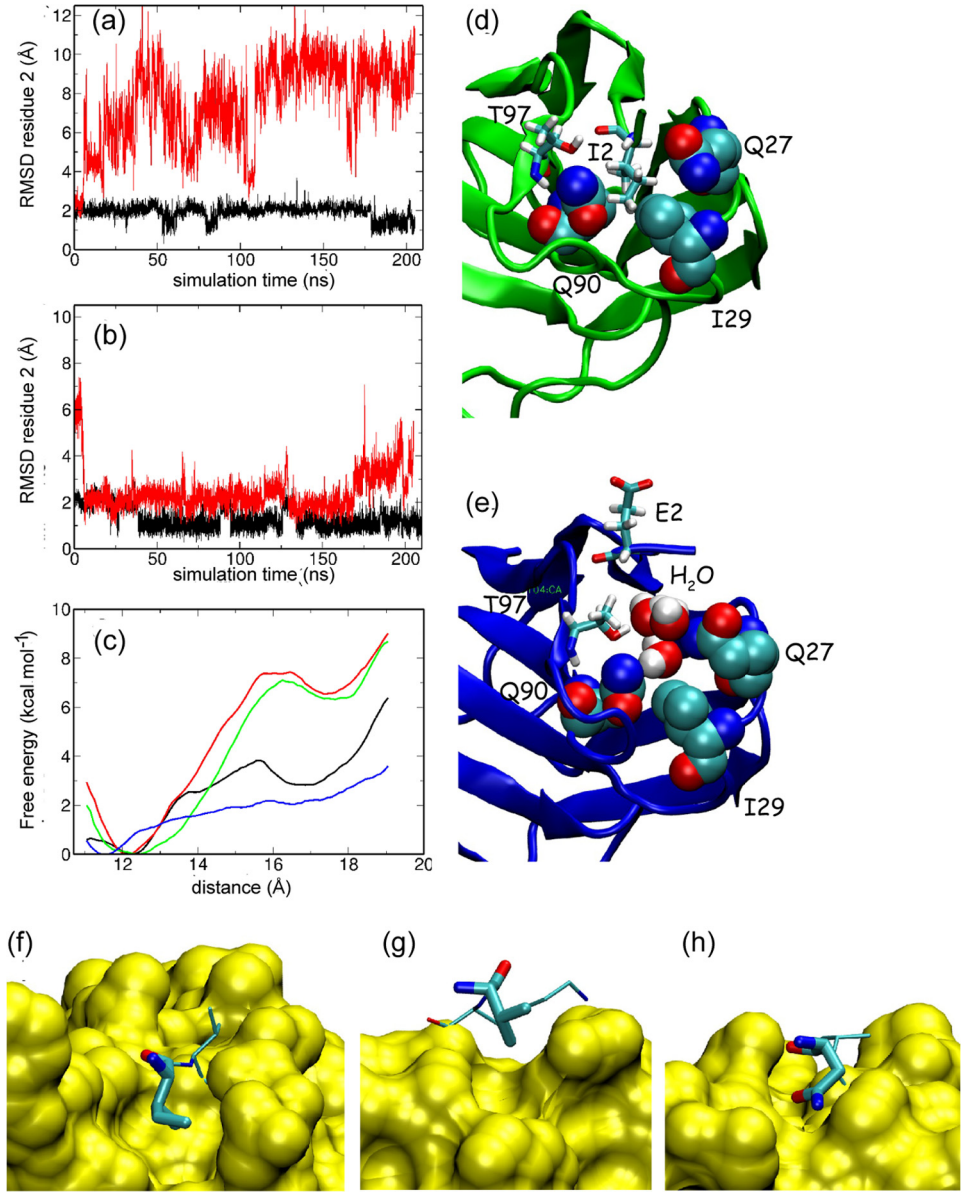

FIGURE 10. Heavy atom r.m.s.d. of residue 2 *versus* simulation time after best superposition on the complete backbone of the start structure for 1OPG $V_L\kappa$-WT (*red*, Glu-2) and 1OPG $V_L\kappa$-E2I (*black*, Ile-2) (*a*) and MAK33 $V_L\kappa$-WT (*black*, Ile-2) and MAK33 $V_L\kappa$-I2E (*red*, Glu-2) (*b*). *c,* calculated potential-of-mean force for the dissociation of the Glu-2 in 1OPG $V_L\kappa$-WT (*black curve*), Ile-2 in 1OPG $V_L\kappa$-E2I (*green*), Ile-2 in MAK33 $V_L\kappa$-WT (*red curve*), and Glu-2 in MAK33 $V_L\kappa$-I2E (*blue curve*) from the hydrophobic cavity region. *d,* N-terminal cavity region of MAK33 $V_L\kappa$ with the Ile-2 side chain buried in the cavity (protein schematic with Ile-2 as sticks model and adjacent side chains as van der Waals spheres). *e,* example of a simulation snapshot with a fully solvent-exposed Glu-2 side chain and several water molecules at the rim of the N-terminal cavity region of 1OPG $V_L\kappa$. *f,* solvent-accessible surface representation in *yellow* of the binding cavity region for residue 2 in the case of MAK33 $V_L\kappa$-WT (stick model of Ile-2); *g.* same for 1VGE V_H-WT with Val-2 as stick representation, and *h,* same for 1AQK $V_L\lambda$-WT with Asn-2.

had lost contacts with the N-terminal cavity region (larger distances resulting in disruption of additional contacts of subsequent residues along the chain). The US simulations indicate a significantly higher dissociation free energy barrier for the case of an Ile at position 2 compared with Glu-2 in both MAK33 and 1OPG $V_L\kappa$ domains. Because in the folded form the Ile-2 residue stays in an associated conformation, one can assign ~2.5 kcal/mol (~10 kJ mol^{-1}) as a free energy difference of dissociation compared with Glu-2 as a folding stabilization free energy contribution of the Ile-2 variants. This is in excellent agreement with our experimental values.

In addition to the $V_L\kappa$ domains, the $V_L\lambda$ and V_H domains (taken from the x-ray structures of 1AQK (49) and 1VGE (39), respectively), were also analyzed. MD simulations were performed starting from the x-ray conformations of the wild type structures and from variants with a Glu at position 2. In all simulations, the domain conformations stayed close (within ~2 Å) to the start structure for a 50-ns sampling time (Fig. 11, *a* and *b*). In the case of 1AQK $V_L\lambda$, the Asn-2 wild type residue is partially solvent-exposed forming contacts with polar and charged residues near the N terminus (Fig. 10*h*). During the simulations, it transiently dissociates to more solvent-exposed states. Similarly, the Glu-2 variant (1AQK $V_L\lambda$-N2E) also shows fluctuations to partially solvent-exposed states with limited contacts to the N-terminal region of the protein (Fig. 11*c*). In the case of 1VGE V_H, residue 2 is in a fully solvent-exposed state

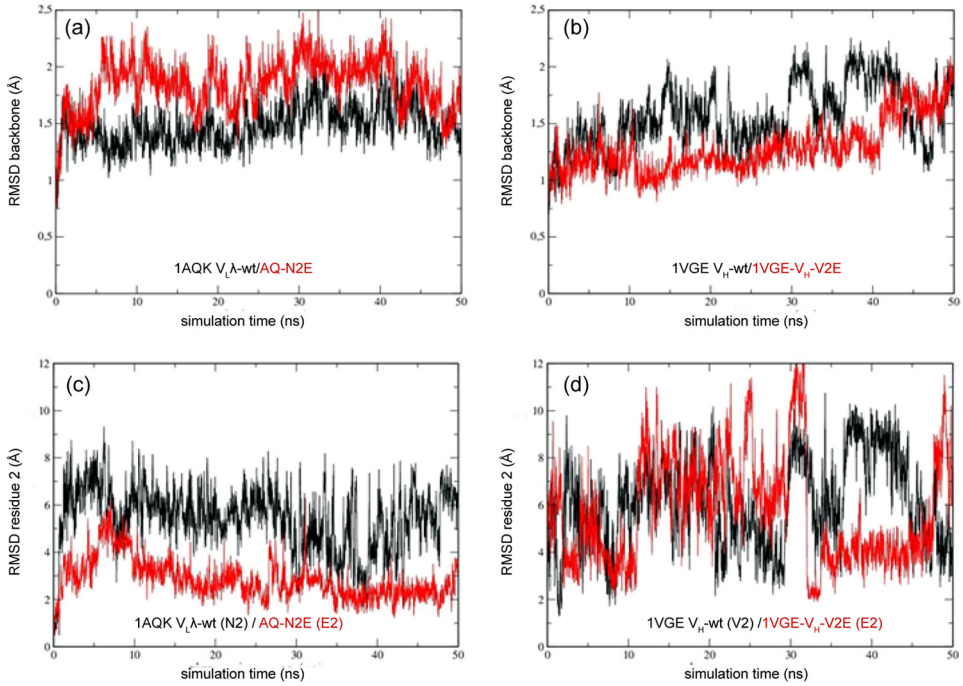

FIGURE 11. *a,* comparison of backbone r.m.s.d. from the corresponding experimental start structure *versus* data gathering simulation time for 1AQK $V_L\lambda$-WT (*black curve*) and 1AQK $V_L\lambda$-N2E (*red curve*). *b,* same for 1VGE V_H-WT (*black curve*) and 1VGE V_H-V2E (*red curve*). Heavy atom r.m.s.d. of residue 2 *versus* simulation time after best superposition on the complete backbone of the start structure for 1AQK $V_L\lambda$-WT (*black*, Asn-2) and 1AQK $V_L\lambda$-N2E (*red*, Glu-2) (*c*) and 1VGE V_H-WT (*black*, Val-2) and 1VGE V_H-V2E (*red*, Glu-2) (*d*).

already in the x-ray starting structure (Fig. 10*g*). No cavity near the N terminus is present that could serve as a stable anchor region for residue 2 as found for the κ domains (Fig. 10*f*). Both the simulations of 1VGE V_H-WT and the V2E mutant showed large fluctuations of residue 2 and no stable binding mode could be identified (Fig. 11*d*). Thus, in these cases neither the wild type nor the Glu-2 variants adopt a stable state with a buried side chain of residue 2 that could contribute to the stability of the protein, in contrast to what was observed for the Ile-2 variants of MAK33 and 1OPG $V_L\kappa$. This is largely due to the absence of an appropriate cavity region near the N terminus and explains why mutation of residue 2 has little or no influence on protein stability in the case of the $V_L\lambda$ and V_H domains.

DISCUSSION

We show here that residue 2 is crucial for the integrity and stability of V_L domains of the κ family, and this residue is a key factor that controls its amyloidogenic properties. Specifically, uncharged residues at position 2 of $V_L\kappa$ domains are important for the maintenance of the structural integrity and a high stability. In agreement with their extremely low frequency in naturally occurring $V_L\kappa$ domains, charged residues do not support this.

During NMR backbone assignment, we encountered several regions that are exchanged-broadened and therefore could not be assigned completely. Interestingly, these regions match well with dynamic residues in the dimer interface of the human $V_L\kappa$ sequence LEN, as identified by Mukherjee *et al.* (51). In this V_L domain (LEN), residues 1–9, 37–58, and 89–100 were shown to exhibit pH-dependent millisecond dynamics, which seem to be related to the process of amyloid fibril formation. The presence of residue 2 within these dynamic regions is another indicator for its relevance for amyloidogenicity. This is supported by our MD simulations that show an increase in N-terminal dynamics caused by a charged residue at position 2. Overall, the I2E substitution affects large parts of the $V_L\kappa$ structure. Both the disruption of the conserved salt bridge and the changes in the hydrophobic core presumably contribute to the loss of thermodynamic stability. However, the short strand-connecting helix (residues 79–83), which is highly conserved in antibody variable domains and known to be important for early folding events of the domain (13) was not affected by the I2E substitution, implying that this replacement may not be involved in the amyloidogenicity of the V_L variants studied here.

Hydrophobic core packing is well known to be an important stabilizing factor in proteins in general (52–54) and antibody domains in particular (55). Therefore, the destabilizing effects of charged residues at position 2 could be explained by the fact that they are energetically unfavorable within the hydrophobic core. A charged residue at position 2 of a $V_L\kappa$ domain leads to a partial exposure of the hydrophobic interior and to the disruption of an optimal packing around residue 2. This in turn causes rearrangements of the whole hydrophobic core region. Consequently, this results in the destabilization of the fold and an increased aggregation propensity. For the $V_L\lambda$ and V_H domains, the residue at position 2 is largely solvent-exposed or forms only transient polar contacts with the surrounding protein surface. In MD simulations, both the wild type residues at position 2 or substitutions with Glu resulted in fluctuating solvent-exposed conformational states due to the lack of a stable binding region. Hence, in the case of the $V_L\lambda$ and V_H domains, residue 2 is not part of the hydrophobic core, and substitution of this residue also does not disrupt the hydrophobic packing of the

domains. Whereas the binding of the N-terminal segment to the hydrophobic cavity is crucial for stability in $V_L\kappa$ domains, it appears to be less important for $V_L\lambda$ and V_H domains. Unlike in the $V_L\kappa$ domains where the hydrophobic cavity requires binding of the N-terminal residue 2 to prevent the unfavorable exposure of nonpolar residues, in the $V_L\lambda$ and V_H domains, the respective hydrophobic cavities are less hydrophobic and do not require binding of residue 2 for protection.

It has been suggested that the formation of amyloid fibrils does not begin from the native state of a protein but more likely from a partially folded state or an intermediate state (32, 56, 57). In this context, the occurrence of particularly nonconservative mutations that involve a change in side chain chemistry in a structurally important region and the correlation with an increased propensity to form amyloid have been reported (32, 58). Mutations and changes in conditions that lead to destabilization of the native state might therefore serve to increase the population of an intermediate state or partially folded species, thereby enabling more molecules to be diverted into an amyloid-forming pathway (59, 60). In this study, the less stable MAK33 and 10PG $V_L\kappa$ variants readily formed fibrils, whereas their stable counterparts did not. Although stability is an important factor determining the amyloidogenic propensity of proteins, the amino acid sequence plays a major role (61) as this determines the amyloid fibril formation kinetics and the types of intermediates populated (13, 32, 56). Although some residues protect against amyloid formation, their chemistry and position within the protein appear to be more important. This protective role is largely attributed to edge strands of β-sheet proteins (62–64). Residue 2 in antibody variable domains appears in β-strand A, which is one of four edge strands (A, D and C″, G) of the β-sandwich topology. Uncharged residues at this position might have evolved to prevent undesirable β-sheet self-propagation (63). The frequent dissociation and solvent exposure of charged residues at position 2 of $V_L\kappa$ domains presumably lead to the disruption of native H-bonds and the subsequent exposure of H-bond donors and acceptors on the edge strand interface. This might result in V_L edge-to-edge aggregation (65). The rare occurrence of charged residues at this position within edge strand A and the high amyloidogenic propensity of these $V_L\kappa$ variants are in line with this explanation. Although there exists a huge similarity between the three different families of variable domains, it has also been shown that they differ significantly in their biophysical properties and propensity to aggregate to amyloid fibrils (55, 66). Our study identifies an important property of the $V_L\kappa$ family, not pertaining to the $V_L\lambda$ and V_H domains, which controls its amyloidogenicity.

A compelling amount of evidence from studies on sequence and structural features that can predispose to amyloid formation has often been limited to given V_L subfamilies (*e.g.* κ1 or λ6) with hardly one feature pertaining to all or an entire variable domain family (67–69). Our results identify a key feature that can destabilize and as a result predispose an entire variable domain family to fibrillar aggregation. The importance of residue 2 for the $V_L\kappa$ family determined here adds to the understanding of antibody LC amyloidosis linking the destabilization of native interactions with amyloid formation. In the context of AL amyloidosis, and also in the broader context of amyloid diseases, however, it remains to be seen whether point mutations promoting fibril formation generally affect stability. It seems reasonable to assume that other mechanisms may also apply.

Acknowledgment—We thank Bettina Richter for excellent technical support.

REFERENCES

1. Schiffer, M. (1996) Molecular anatomy and the pathological expression of antibody light chains. *Am. J. Pathol.* **148,** 1339–1344
2. Halaby, D. M., and Mornon, J. P. (1998) The immunoglobulin superfamily: an insight on its tissular, species, and functional diversity. *J. Mol. Evol.* **46,** 389–400
3. Buxbaum, J., and Gallo, G. (1999) Nonamyloidotic monoclonal immunoglobulin deposition disease. Light-chain, heavy-chain, and light- and heavy-chain deposition diseases. *Hematol. Oncol. Clin. North Am.* **13,** 1235–1248
4. Pozzi, C., D'Amico, M., Fogazzi, G. B., Curioni, S., Ferrario, F., Pasquali, S., Quattrocchio, G., Rollino, C., Segagni, S., and Locatelli, F. (2003) Light chain deposition disease with renal involvement: clinical characteristics and prognostic factors. *Am. J. Kidney Dis.* **42,** 1154–1163
5. Kyle, R. A., and Gertz, M. A. (1995) Primary systemic amyloidosis: clinical and laboratory features in 474 cases. *Semin. Hematol.* **32,** 45–59
6. Blancas-Mejía, L. M., and Ramirez-Alvarado, M. (2013) Systemic amyloidoses. *Annu. Rev. Biochem.* **82,** 745–774
7. Pepys, M. B. (2006) Amyloidosis. *Annu. Rev. Med.* **57,** 223–241
8. Buxbaum, J. N., Chuba, J. V., Hellman, G. C., Solomon, A., and Gallo, G. R. (1990) Monoclonal immunoglobulin deposition disease: light chain and light and heavy chain deposition diseases and their relation to light chain amyloidosis. Clinical features, immunopathology, and molecular analysis. *Ann. Intern. Med.* **112,** 455–464
9. Falk, R. H., Comenzo, R. L., and Skinner, M. (1997) The systemic amyloidoses. *N. Engl. J. Med.* **337,** 898–909
10. Dispenzieri, A., Gertz, M. A., and Buadi, F. (2012) What do I need to know about immunoglobulin light chain (AL) amyloidosis? *Blood Rev.* **26,** 137–154
11. Merlini, G., and Palladini, G. (2008) Amyloidosis: is a cure possible? *Ann. Oncol.* **19,** Suppl. 4, 63–66
12. Miyazaki, D., Yazaki, M., Gono, T., Kametani, F., Tsuchiya, A., Matsuda, M., Takenaka, Y., Hosh, Y., 2nd, and Ikeda, S. (2008) AH amyloidosis associated with an immunoglobulin heavy chain variable region (VH1) fragment: a case report. *Amyloid* **15,** 125–128
13. Feige, M. J., Groscurth, S., Marcinowski, M., Yew, Z. T., Truffault, V., Paci, E., Kessler, H., and Buchner, J. (2008) The structure of a folding intermediate provides insight into differences in immunoglobulin amyloidogenicity. *Proc. Natl. Acad. Sci. U.S.A.* **105,** 13373–13378
14. Pace, C. N. (1986) Determination and analysis of urea and guanidine hydrochloride denaturation curves. *Methods Enzymol.* **131,** 266–280
15. Simpson, E. R., Herold, E. M., and Buchner, J. (2009) The folding pathway of the antibody V(L) domain. *J. Mol. Biol.* **392,** 1326–1338
16. Feige, M. J., Simpson, E. R., Herold, E. M., Bepperling, A., Heger, K., and Buchner, J. (2010) Dissecting the alternatively folded state of the antibody Fab fragment. *J. Mol. Biol.* **399,** 719–730
17. Feige, M. J., Walter, S., and Buchner, J. (2004) Folding mechanism of the CH2 antibody domain. *J. Mol. Biol.* **344,** 107–118
18. Feige, M. J., Hagn, F., Esser, J., Kessler, H., and Buchner, J. (2007) Influence of the internal disulfide bridge on the folding pathway of the CL antibody domain. *J. Mol. Biol.* **365,** 1232–1244
19. Santoro, M. M., and Bolen, D. W. (1988) Unfolding free energy changes determined by the linear extrapolation method. 1. Unfolding of phenylmethanesulfonyl α-chymotrypsin using different denaturants. *Biochemistry* **27,** 8063–8068
20. Doty, P., and Steiner, R. F. (1950) Light scattering and spectrophotometry of colloidal solutions. *J. Chem. Phys.* **18,** 1211–1220
21. Vetri, V., Canale, C., Relini, A., Librizzi, F., Militello, V., Gliozzi, A., and

Leone, M. (2007) Amyloid fibrils formation and amorphous aggregation in concanavalin A. *Biophys. Chem.* **125,** 184–190
22. Sattler, M., Schleucher, J., and Griesinger, C. (1999) Heteronuclear multidimensional NMR experiments for the structure determination of proteins in solution employing pulsed field gradients. *Prog. Nuclear Magn. Reson. Spectrosc.* **34,** 93–158
23. Vranken, W. F., Boucher, W., Stevens, T. J., Fogh, R. H., Pajon, A., Llinas, M., Ulrich, E. L., Markley, J. L., Ionides, J., and Laue, E. D. (2005) The CCPN data model for NMR spectroscopy: development of a software pipeline. *Proteins* **59,** 687–696
24. Guex, N., Diemand, A., and Peitsch, M. C. (1999) Protein modelling for all. *Trends Biochem. Sci.* **24,** 364–367
25. Case, D. A., Darden, T. A., Cheatham, T. E., Simmerling, C. Wang, J., Duke, R. E., Luo, R., Walker, R. C., Zhang, W., Merz, K. M., Roberts, B., Hayik, S., Roitberg, A., Seabra, G., Swails, J., Goetz, A. W., Kolossvary, I., Wong, K. F., Paesani, F., Vanicek, J., Wolf, R. M., Liu, J., Wu, X., Brozell, S. R., Steinbrecher, T., Gohlke, H., Cai, Q., Ye, X., Wang, J., Hsieh, M. J., Cui, G., Roe, D. R., Mathews, D. H., Seetin, M. G., Salomon-Ferrer, R., Sagui, C., Babin, V., Luchko, T., Gusarov, S., Kovalenko, A., and Kollman, P. A. (2012) *Amber12*, University of California, San Francisco
26. Jorgensen, W. L., Chandrasekhar, and Madura, J. D. (1983) Comparison of simple potential functions for simulating liquid water. *J. Chem. Phys.* **79,** 926–935
27. Kumar, S., Bouzida, D., Swendsen, R. H., Kollman, P. A., and Rosenberg, J. M. (1992) The weighted histogram analysis method for free-energy calculations on biomolecules. The method. *J. Comput. Chem.* **13,** 1011–1021
28. Augustine, J. G., de La Calle, A., Knarr, G., Buchner, J., and Frederick, C. A. (2001) The crystal structure of the fab fragment of the monoclonal antibody MAK33. Implications for folding and interaction with the chaperone bip. *J. Biol. Chem.* **276,** 3287–3294
29. Kodandapani, R., Veerapandian, B., Kunicki, T. J., and Ely, K. R. (1995) Crystal structure of the OPG2 Fab. An antireceptor antibody that mimics an RGD cell adhesion site. *J. Biol. Chem.* **270,** 2268–2273
30. Buchner, J., Renner, M., Lilie, H., Hinz, H. J., Jaenicke, R., Kiefhabel, T., and Rudolph, R. (1991) Alternatively folded states of an immunoglobulin. *Biochemistry* **30,** 6922–6929
31. Lilie, H., and Buchner, J. (1995) Domain interactions stabilize the alternatively folded state of an antibody Fab fragment. *FEBS Lett.* **362,** 43–46
32. Hurle, M. R., Helms, L. R., Li, L., Chan, W., and Wetzel, R. (1994) A role for destabilizing amino acid replacements in light-chain amyloidosis. *Proc. Natl. Acad. Sci. U.S.A.* **91,** 5446–5450
33. Raffen, R., Dieckman, L. J., Szpunar, M., Wunschl, C., Pokkuluri, P. R., Dave, P., Wilkins Stevens, P., Cai, X., Schiffer, M., and Stevens, F. J. (1999) Physicochemical consequences of amino acid variations that contribute to fibril formation by immunoglobulin light chains. *Protein Sci.* **8,** 509–517
34. Fändrich, M., and Dobson, C. M. (2002) The behaviour of polyamino acids reveals an inverse side chain effect in amyloid structure formation. *EMBO J.* **21,** 5682–5690
35. Dobson, C. M. (2003) Protein folding and misfolding. *Nature* **426,** 884–890
36. Chiti, F., Taddei, N., Baroni, F., Capanni, C., Stefani, M., Ramponi, G., and Dobson, C. M. (2002) Kinetic partitioning of protein folding and aggregation. *Nat. Struct. Biol.* **9,** 137–143
37. Johnson, G., and Wu, T. T. (2000) Kabat database and its applications: 30 years after the first variability plot. *Nucleic Acids Res.* **28,** 214–218
38. Lefranc, M. P. (2003) IMGT, the international ImMunoGeneTics database. *Nucleic Acids Res.* **31,** 307–310
39. Chacko, S., Padlan, E. A., Portolano, S., McLachlan, S. M., and Rapoport, B. (1996) Structural studies of human autoantibodies. Crystal structure of a thyroid peroxidase autoantibody Fab. *J. Biol. Chem.* **271,** 12191–12198
40. Ohhashi, Y., Kihara, M., Naiki, H., and Goto, Y. (2005) Ultrasonication-induced amyloid fibril formation of β2-microglobulin. *J. Biol. Chem.* **280,** 32843–32848
41. Chatani, E., Lee, Y. H., Yagi, H., Yoshimura, Y., Naiki, H., and Goto, Y. (2009) Ultrasonication-dependent production and breakdown lead to minimum-sized amyloid fibrils. *Proc. Natl. Acad. Sci. U.S.A.* **106,** 11119–11124
42. So, M., Yagi, H., Sakurai, K., Ogi, H., Naiki, H., and Goto, Y. (2011) Ultrasonication-dependent acceleration of amyloid fibril formation. *J. Mol. Biol.* **412,** 568–577
43. Yagi, H., Hasegawa, K., Yoshimura, Y., and Goto, Y. (2013) Acceleration of the depolymerization of amyloid β fibrils by ultrasonication. *Biochim. Biophys. Acta* **1834,** 2480–2485
44. Kitayama, H., Yoshimura, Y., So, M., Sakurai, K., Yagi, H., and Goto, Y. (2013) A common mechanism underlying amyloid fibrillation and protein crystallization revealed by the effects of ultrasonication. *Biochim. Biophys. Acta* **1834,** 2640–2646
45. Yoshimura, Y., Matsumoto, S., Hisashi, Y., and Yuji, G. (2013) Ultrasonication: an efficient agitation for accelerating the supersaturation-limited amyloid fibrillation of proteins. *Jpn. J. Appl. Phys.* **52,** 07HA01-07HA01-08
46. LeVine, H., 3rd (1993) Thioflavine T interaction with synthetic Alzheimer's disease β-amyloid peptides: detection of amyloid aggregation in solution. *Protein Sci.* **2,** 404–410
47. Khurana, R., Coleman, C., Ionescu-Zanetti, C., Carter, S. A., Krishna, V., Grover, R. K., Roy, R., and Singh, S. (2005) Mechanism of thioflavin T binding to amyloid fibrils. *J. Struct. Biol.* **151,** 229–238
48. Chiba, T., Hagihara, Y., Higurashi, T., Hasegawa, K., Naiki, H., and Goto, Y. (2003) Amyloid fibril formation in the context of full-length protein: effects of proline mutations on the amyloid fibril formation of β2-microglobulin. *J. Biol. Chem.* **278,** 47016–47024
49. Faber, C., Shan, L., Fan, Z., Guddat, L. W., Furebring, C., Ohlin, M., Borrebaeck, C. A., and Edmundson, A. B. (1998) Three-dimensional structure of a human Fab with high affinity for tetanus toxoid. *Immunotechnology* **3,** 253–270
50. Wu, T. T., and Kabat, E. A. (1970) An analysis of the sequences of the variable regions of Bence Jones proteins and myeloma light chains and their implications for antibody complementarity. *J. Exp. Med.* **132,** 211–250
51. Mukherjee, S., Pondaven, S. P., and Jaroniec, C. P. (2011) Conformational flexibility of a human immunoglobulin light chain variable domain by relaxation dispersion nuclear magnetic resonance spectroscopy: implications for protein misfolding and amyloid assembly. *Biochemistry* **50,** 5845–5857
52. Pace, C. N. (1990) Measuring and increasing protein stability. *Trends Biotechnol.* **8,** 93–98
53. Billings, K. S., Best, R. B., Rutherford, T. J., and Clarke, J. (2008) Crosstalk between the protein surface and hydrophobic core in a core-swapped fibronectin type III domain. *J. Mol. Biol.* **375,** 560–571
54. Benítez-Cardoza, C. G., Stott, K., Hirshberg, M., Went, H. M., Woolfson, D. N., and Jackson, S. E. (2004) Exploring sequence/folding space: folding studies on multiple hydrophobic core mutants of ubiquitin. *Biochemistry* **43,** 5195–5203
55. Ewert, S., Huber, T., Honegger, A., and Plückthun, A. (2003) Biophysical properties of human antibody variable domains. *J. Mol. Biol.* **325,** 531–553
56. Kelly, J. W. (1998) The alternative conformations of amyloidogenic proteins and their multi-step assembly pathways. *Curr. Opin Struct. Biol.* **8,** 101–106
57. Uversky, V. N., and Fink, A. L. (2004) Conformational constraints for amyloid fibrillation: the importance of being unfolded. *Biochim. Biophys. Acta* **1698,** 131–153
58. Poshusta, T. L., Sikkink, L. A., Leung, N., Clark, R. J., Dispenzieri, A., and Ramirez-Alvarado, M. (2009) Mutations in specific structural regions of immunoglobulin light chains are associated with free light chain levels in patients with AL amyloidosis. *PLoS One* **4,** e5169
59. Bellotti, V., Mangione, P., and Merlini, G. (2000) Review: immunoglobulin light chain amyloidosis–the archetype of structural and pathogenic variability. *J. Struct. Biol.* **130,** 280–289
60. Souillac, P. O., Uversky, V. N., Millett, I. S., Khurana, R., Doniach, S., and Fink, A. L. (2002) Effect of association state and conformational stability on the kinetics of immunoglobulin light chain amyloid fibril formation at physiological pH. *J. Biol. Chem.* **277,** 12657–12665
61. Chiti, F., Stefani, M., Taddei, N., Ramponi, G., and Dobson, C. M. (2003) Rationalization of the effects of mutations on peptide and protein aggregation rates. *Nature* **424,** 805–808
62. Jones, S., Smith, D. P., and Radford, S. E. (2003) Role of the N- and C-ter-

minal strands of β2-microglobulin in amyloid formation at neutral pH. *J. Mol. Biol.* **330,** 935–941
63. Richardson, J. S., and Richardson, D. C. (2002) Natural β-sheet proteins use negative design to avoid edge-to-edge aggregation. *Proc. Natl. Acad. Sci. U.S.A.* **99,** 2754–2759
64. Monsellier, E., and Chiti, F. (2007) Prevention of amyloid-like aggregation as a driving force of protein evolution. *EMBO Rep.* **8,** 737–742
65. Nowak, M. (2004) Immunoglobulin κ light chain and its amyloidogenic mutants: a molecular dynamics study. *Proteins* **55,** 11–21
66. Dudgeon, K., Rouet, R., Kokmeijer, I., Schofield, P., Stolp, J., Langley, D., Stock, D., and Christ, D. (2012) General strategy for the generation of human antibody variable domains with increased aggregation resistance. *Proc. Natl. Acad. Sci. U.S.A.* **109,** 10879–10884
67. Comenzo, R. L., Zhang, Y., Martinez, C., Osman, K., and Herrera, G. A. (2001) The tropism of organ involvement in primary systemic amyloidosis: contributions of Ig V(L) germ line gene use and clonal plasma cell burden. *Blood* **98,** 714–720
68. Perfetti, V., Casarini, S., Palladini, G., Vignarelli, M. C., Klersy, C., Diegoli, M., Ascari, E., and Merlini, G. (2002) Analysis of V(λ)-J(λ) expression in plasma cells from primary (AL) amyloidosis and normal bone marrow identifies 3r (λIII) as a new amyloid-associated germline gene segment. *Blood* **100,** 948–953
69. Abraham, R. S., Geyer, S. M., Price-Troska, T. L., Allmer, C., Kyle, R. A., Gertz, M. A., and Fonseca, R. (2003) Immunoglobulin light chain variable (V) region genes influence clinical presentation and outcome in light chain-associated amyloidosis (AL). *Blood* **101,** 3801–3808

A Residue-specific Shift in Stability and Amyloidogenicity of Antibody Variable Domains

Cardine N. Nokwe, Martin Zacharias, Hisashi Yagi, Manuel Hora, Bernd Reif, Yuji Goto and Johannes Buchner

J. Biol. Chem. 2014, 289:26829-26846.
doi: 10.1074/jbc.M114.582247 originally published online August 5, 2014
